Theory and Fabrication of Evanescently-Coupled
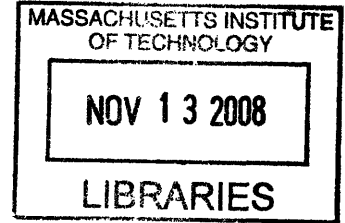# Photoluminescent Devices

by

David Harry Friend

Submitted to the Department of Electrical Engineering and Computer
Science
in partial fulfillment of the requirements for the degree of

Masters of Engineering in Electrical Engineering

at the

MASSACHUSETTS INSTITUTE OF TECHNOLOGY

June 2008

© Massachusetts Institute of Technology 2008. All rights reserved.

Author . . . .
Department of Electrical Engineering and Computer Science
May 12, 2008

Certified by . . . .
Vladimir Bulović
Associate Professor of Electrical Engineering and Computer Science
Thesis Supervisor

Accepted by . . . . _   . . . .
Arthur C. Smith
Chairman, Department Committee on Graduate Students

Theory and Fabrication of Evanescently-Coupled Photoluminescent Devices

by

David Harry Friend

Abstract

This thesis discusses the theory and implementation of evanescently-coupled photo-luminescent devices. We demonstrate the feasibility of efficient, spectrally tunable lighting devices through quantum dot photoluminescence.

Devices that enjoy both great efficiencies and excellent color temperatures are the goal of current lighting research. They are a "have your cake and eat it too," achievement that are not realized with current technologies.

It has long been recognized that the narrow and tunable emission spectra of quantum dots allows access to an unprecedented range of colors, with which one could construct a spectrally perfect white light. However, current quantum dot photoluminescent devices suffer efficiency losses due to high reabsorption of emitted light. We demonstrate that the idea of evanescent coupling permits use of a thin film geometry, whereby thick films and their associated inefficiencies can be avoided. Specifically, QDs are stabilized in the cladding of a waveguide and excited by the evanescent field of the guided modes rather than by direction illumination. As an additional advantage, the pump light and emission can be spatially distant; this decoupling promises to alleviate engineering headaches related to heat dissipation.

Thesis Supervisor: Vladimir Bulović
Title: Associate Professor of Electrical Engineering and Computer Science

Acknowledgments

In memory of EV and RW who join me in toasting לחיים. Toasts to:

- My wonderful family, and the rest of the **Robins**, who allowed my curiosity to fester, unchecked: I guess you've had your $200K wake-up call. That's what you get when you make your child assemble his own toys at Christmas.

- My **brothers**: although your five years of comedy coaching have shown limited results, they have impressed upon me the lifelessness of resolute sincerity. yf.

- **Jon**: everything that I know about chemistry I learned from you. MIT-EHS is scared.

- **Cliff**: thanks for putting up with my shenanigans.

- **Ellie**: some advice: don't make a habit of Charles River showers.

- **Prof. Moungi Bawendi** and **Prof. Vladimir Bulovic**: I hope you're not reading this page.

- **looe** and **nanocluster**, especially **Lisa**, **Yakkov**, **Scott**, **Gerry**, and **Polly**: your discussions have been invaluable. I've concluded that the brown Expo markers do smell better than the black ones.

- **You**, the anonymous reader: Thank you. Seriously. You might be the only one.

Contents

List of Figures

List of Tables

Chapter 1

Introduction

This thesis describes efforts to incorporate highly fluorescent semiconductor nanocrystals (quantum dots) into the cladding of an optical waveguide to realize photoluminescence through the evanescent field of guided modes. As discussed below, the design has several advantages over current implementations that directly irradiate the fluorescent materials. Following this introductory chapter, the thesis is divided into two parts. Chapters 2 and 3 present the theory, while Chapter 4 presents implementation efforts. Specifically, Chapter 2 delves extensively into the optical theory of waveguides and evanescent coupling. The derived results guide our design choices. By contrast, Chapter 3 is a cursory introduction to the theory and synthesis of quantum dots, which are not unique to this thesis. In the second half, efforts to fabricate devices are detailed in Chapter 4. Finally, Chapter 5 offers a short overall conclusion to the thesis and a note on the future outlook of these endeavors.

1.1 Overview

We present an novel idea for a white solid state lighting device that has both a high external quantum efficiency and excellent color temperature. Light is produced through the photoluminescence (PL) of quantum dots (QDs) that are coupled to the evanescent field of waveguided pump light.

Specific advantages of QDs over organic phosphors include their range of emission

frequencies, their greater stability, and their high density of absorbing states. With proper synthetic design, the PL efficiency of a QD can exceed 90%, and the emission wavelength can be tuned to all visible colors. Careful selection of multiple QD colors will generate highly efficient white lights of arbitrary color temperature and high color rendering index (CRI).
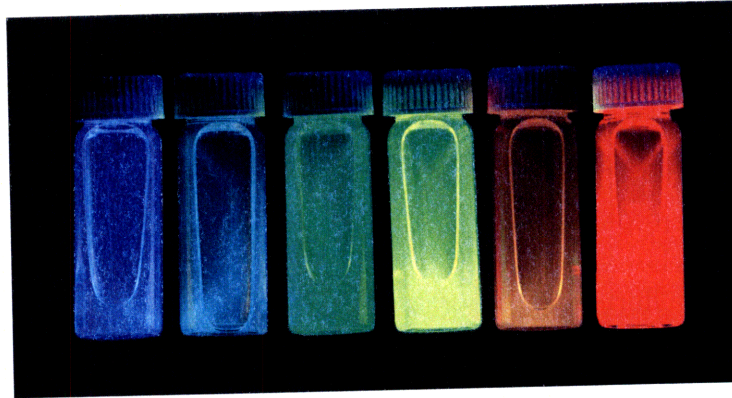
Figure 1-1: Colloidal CdSe quantum dots dissolved in hexane and pumped by a UV light. Smaller dots enforce higher confinement of the exciton and blue shift the emission frequency from the bulk CdSe bandgap. Emission color can be controlled through both semiconductor material choice and core size. Dots can be mixed to achieve the desired non-spectral color. Photo by F. Frankel.

Previous attempts to utilize QDs for downconversion have failed to produce highly efficient devices due to large reabsorption in optical device geometries containing thick QD films. In contrast, we demonstrate (Figure 1-2) that the photoluminescence can be achieved using a thin QD coating on an optical waveguide. The pump light, a green laser in the figure, is coupled into the fiber. The evanescent field of the guided pump light is absorbed by the thin film of (CdSe)ZnS QDs embedded a silica sol-gel, resulting in QD radiation at $\lambda = 609$ nm. In this preparation, the polymer cladding of the fiber was mechanically stripped, and the naked 200 μm silica core was dip coated into a sol-gel precursor containing (CdSe)ZnS QDs. Application of heat gelled the solution. The resulting film is highly robust to chemical and physical etchants.

There are two problems with using a fiber waveguide: (1) only a small fraction of the pump light is used—the majority spills out at the end of the fiber; and, (2) up to 80% of the emission couples back into the waveguide. This thesis proposes a
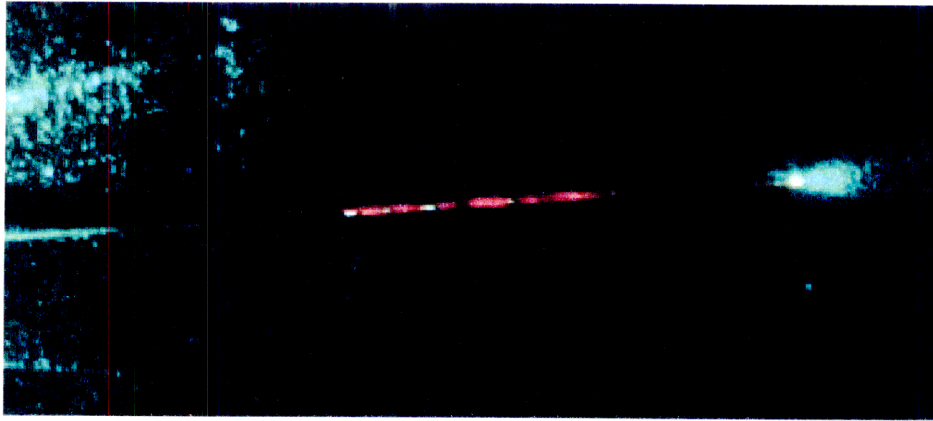
Figure 1-2: Photograph of luminescent fiber pumped by a 514 nm laser. The evanescent field of the propagating modes couples with 609 nm QDs embedded in a silica sol-gel. Only a small fraction of the pump light couples into the QDs; the rest spills out at the end of the fiber. Photo by Cliff R. Wong.

(a) Top-down view

(b) Side profile
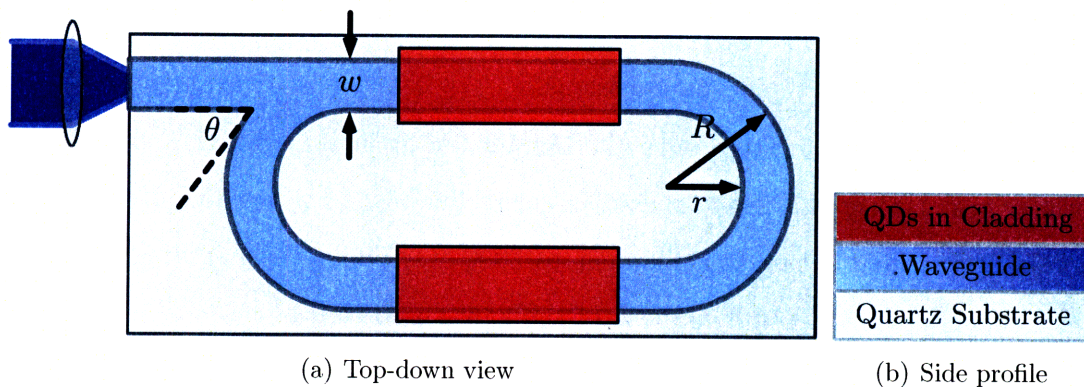
Figure 1-3: Proposed lighting device. The device glows in the regions coated with quantum dots, shown here in red. Marked are critical dimensions and a lens-coupled excitation source.

solution to both problems. First we utilize a Q-shaped waveguide to recycle the pump light until complete attenuation. Such a design is sketched in Figure 1-3. Second, we propose that a photonic crystal structure will greatly improve the efficiency of the device by creating a bandgap in the waveguide. Photons with frequencies in the bandgap cannot propagate through the guide. By tuning the crystal periodicity to the wavelength of the emitted light, we can scatter the QD emission from the waveguide.

1.2 Background and Motivation

There are three considerations for the overall quality of a lighting device; these are important to set out if we claim to be producing a "better" light. The first is efficiency, or the energy loss associated with converting electric power into visible photons. The second is color quality, or how well the light's spectra matches that of the sun, which is considered the ideal white. The final measure is the robustness the device, which includes both fragility and longevity.

1.2.1 Efficiency and Robustness

A 2002 study, as reported by the U.S. Department of Energy, estimated that artificial lighting consumes 8% of U.S. energy and 22% of U.S. electricity [44]. The energy cost is estimated at $50B annually, or $200 per year per capita. Artificial lighting contributes to 8% of U.S. carbon emissions.

The energy cost associated with the ubiquity of artificial lighting is exacerbated by the continued use of Edison's incandescent technology, in which 95% of the energy is expended to heat a tungsten filament to 3000 °C. Only 5% is emitted as visible light.[1] Incandescents account for 12% of the lights used today.

To be fair, alternative technologies are in use. Fluorescents are remarkably more efficient, with a full 20% conversion efficiency, and account for 62% of the light bulbs used today. Finally, HID lamps (such as street lamps), round out the remaining 26% of light bulbs at 25% efficiency. By contrast, electric motors are 85-90% efficient [44].

This thesis describes research in the area of solid state lighting (SSL). Current SSL technology, such as white LEDs, have efficiencies of 35%. If, by 2025, half of all lighting installations used solid-state technologies, the effects would be striking. The US would use 62% less electricity than the currently predicted 1000 TW for a savings of $42B per year. Such a change would alleviate the need to build 70 nuclear power plants to meet increased demand [44].

---

[1] America does slightly better than the rest of the world in this respect. Driving an incandescent at 220 V versus the US standard of 120 V is even less efficient.

Another advantage of SSL is robustness. Incandescent and fluorescent bulbs are rated for thousands of hours of use. (The US consumes 1.5 billion light bulbs each year.) By contrast, LEDs will run for tens of thousands of hours. Longevity promises to be a boon for cities which must employ crews to replace street lamps at high labor and fuel costs. An additional advantage: SSL devices are packaged in unbreakable plastics and metals.

1.2.2 Color Quality of a Lighting Device

The quality of the light is commonly measured with reference to the CIE color space. The CIE color space is the result of research done by W. D. Wright in 1928 and by J. Guild in 1931 on human perception of color. They discovered metamerism: that two light sources may be made from different mixtures of spectral colors, and have the same apparent hue. The CIE color space standardizes this phenomenon: mixtures of sources that have the same apparent hue map to the same coordinates in the color space, regardless of the spectral ingredients.

In the CIE color space, hues are mapped to projective coordinates (x, y). Figure 1-4(a) shows the resulting chromaticity diagram, which is the color gamut for the typical human eye. The locus of visible monochromatic spectral colors form the outer boundary of the color triangle. Ideal white appears in the middle at $(x, y) = (0.33, 0.33)$.

With two sources corresponding to two different points within the gamut, one can make all hues on the line connecting those two points by changing the relative intensity of the two sources. It follows that, given three non-collinear sources, all hues within the constructed triangle can be formed through the proper intensity adjustment of the vertices.

Note that there are no three points that enclose the entire gamut. Expanding to four allows access to more of the gamut, and the de facto standard is eight unsaturated colors. However, because of the concavity of the space, the gamut cannot be covered by a finite number of real sources. Only blackbody emitters contain the infinite number of sources necessary to span the color gamut. Current QD fabrication techniques allow us to access 80% of the gamut (Figure 1-4(b)).

17

(a) CIE color space   (b) QD luminescence in color space
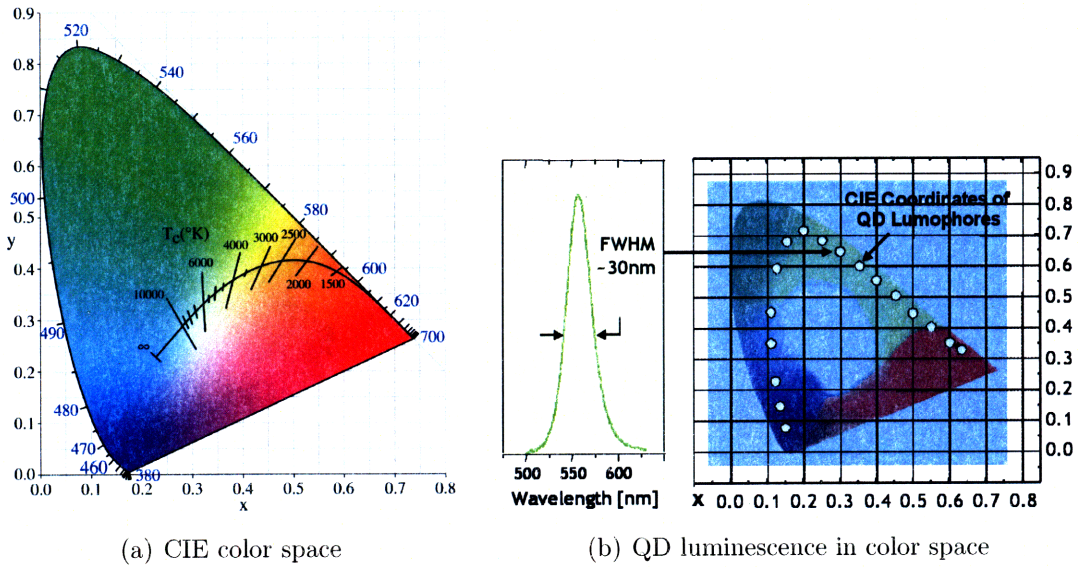
Figure 1-4: CIE 1931 color space chromaticity diagram based on derived coordinates x and y. The locus of spectral colors forms the outer boundary (shown as wavelengths in nm). The curve through center is the Planckian locus and shows human perception of the color of blackbody emitters at various temperatures. Perfect white lies on this locus and is defined by the temperature of the Sun (5500 K).

Given the CIE color space, there are two measures of light quality. The first is the color rendering index (CRI) which ranges from 0 to 100. The CRI describes how well colors are rendered when illuminated with the light under test and is closely related to how many monochromatic sources are present in the illumination source. It is assumed that colors rendered by sunlight illumination are "correct"; sunlight has a CRI of 100. A monochromatic source has a CRI of 0. For comparison, cool white fluorescent lamps have a CRI of 63. Newer triphosphor fluorescent lamps have CRIs of 80 to 90. Modern incandescent bulbs such as halogens have CRIs in the high 90's because they are blackbodies and emit at many different wavelengths.

The second measure of light quality is color temperature. The black curve through the middle of Figure 1-4(a) is the chromaticity of blackbody emitters at various temperatures. A very hot blackbody appears blueish to our eyes. The Sun[2] is again the standard, behaving as a blackbody with a temperature of $T = 5500$ K and appears

---

[2] As a physicist, I feel compelled to add that the Sun is *not* a blackbody at high frequencies because the surface temperature is not uniform. But in the range of the visible spectrum, the blackbody approximation is an excellent one.

white to our eyes. Finally, a cold (cold is a relative term) blackbody looks reddish or even infrared (black). Paradoxically, we describe tungsten incandescents as "warm" lights, even though they are actually too cold.

It is in color quality that our design excels over current SSL devices. To create white LEDs, manufacturers start with blue and add phosphors such as YAG to downconvert some of the blue light into yellow. The spectral mix of blue and yellow appears white to the eye. For higher CRI, multiple phosphors can be used.

(a) YAG Phosphor LED   (b) Quantum Dot LED
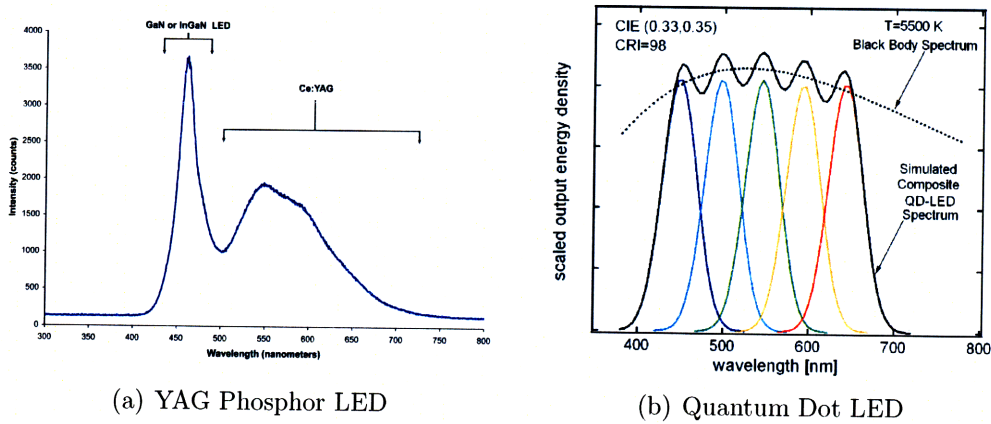
Figure 1-5: Emission spectrum of a white QD-LED compared to that of a white YAG LED. The CRI of the QD-LED is significantly higher because we are able to precisely tune the emission peaks.

QDs are an attractive replacement for the down-converting phosphors because they are more stable, have higher efficiencies, and their emission can be precisely tuned. By mixing QDs we can generate any desired spectrum with high precision. This quality is illustrated in Figure 1-5.

1.3   Novelty of Our Idea

Current LED Technology

To create a white LED using QDs, one could imagine a design similar to that shown in Figure 1-6(a). The QDs absorb the UV light and emit the desired spectra [30]. We can play all of the normal tricks to increase light extraction [29]. In short, this design is a normal LED where QDs substitute for the normal phosphors.

However, the design is inefficient because it allows for excessive reabsorption of the emitted light. Because QDs have a small Stokes' shift (~ 2 nm), the emission from one QD can be easily reabsorbed by another QD, even in a nearly monodisperse popoulation. Every emission/absorption cycle not only decreases the efficiency of the device by a factor equal to the quantum efficiency of the QDs, but also red-shifts the final spectrum. In effect, we see emission from only the largest dots. An extreme example of this red shift is shown in Figure 1-6. A quantitative look at the red-shift is explored in Figure 1-7.

(a) Schematic   (b) LED without QDs   (c) LED with QD
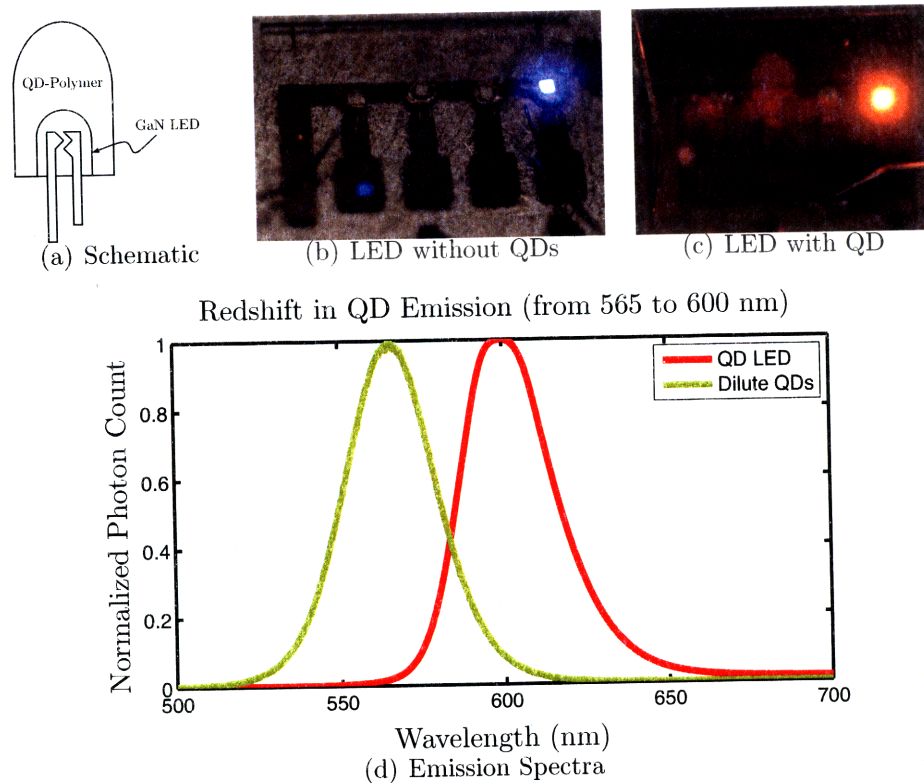
(d) Emission Spectra

Figure 1-6: A poor design for using QDs as the down-converting element of LEDs. (a) schematic of device, (b) GaN LED without dots, (c) GaN LED with dots, (d) redshift of dot spectra. Due to the thick film structure, much of the QD emission is reabsorbed by other QDs, reducing the external quantum efficiency. For the device depicted here, the LED backlight is 460 (blue) and the dots emit at 565 nm. The peak has been redshifted by high concentration to 600.
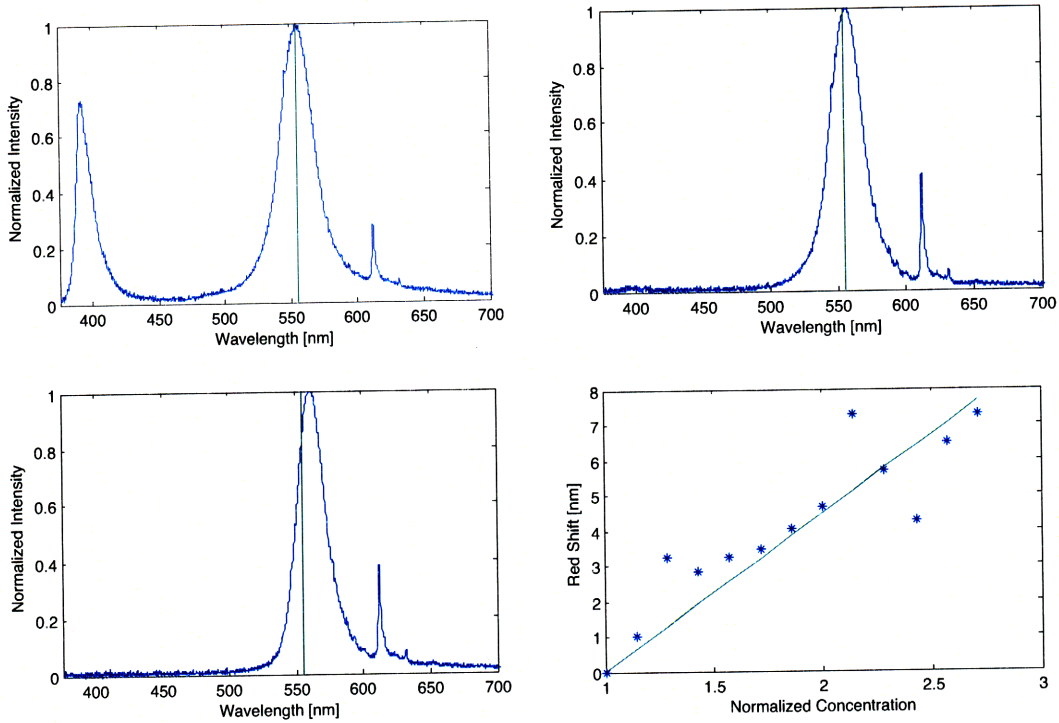
Figure 1-7: Red shift due to reasorption of dots. Shown are three emission spectra from the device shown in Figure 1-6(a). The dots emit at 555 nm, which is marked with a green line in the spectral plots. The fourth plot shows the locally linear relationship between dot concentration and red shift of the emission peak due to absorption-reemision. (a) has a normalized concentration of 1x, (b) is 1.5x, and (c) is 3x. Excitation is at 395 nm. The peak at 612 nm is background noise from room lights. Plot (b) is optimal; at 1.5x concentration the UV backlight is completely absorbed but the red-shift is minimal.

A New Device

We propose an entirely new excitation system that uses a thin QD film to eliminate the reabsorption problem. Rather than pumping the QDs with direct illumination, we propose that the QDs be embedded into the cladding of a waveguide. The QDs will couple to the pump light through the evanescent field of the waveguide. A few other researchers have used evanescent coupling, but none for application to SSL [35, 14, 19].

This thesis traces several iterations of the basic design of embedding QDs into the cladding of a waveguide. The first step was a QD film coated onto the core of an optical fiber, the result of which is shown in Figure 1-2. A sample of (CdSe)ZnS QDs were embedded into a silica sol-gel solution. The cladding of the fiber was

mechanically removed and the sol-gel was drop cast onto the silica core. When cured, the sol-gel material was very stable. The refractive index of the core is identical within a fraction of a percent to the refractive index of the silica sol-gel, and a significant portion of the energy of the guided modes extends into the cladding, exciting the QDs.

The drawback of the fiber waveguide is that most of the pump light is wasted. This thesis explores a Q-shaped waveguide as a means of recycling the pump light (Figure 1-3). Waveguide branching has been widely characterized, and such a shape has been employed by [12]. The relevant parameter is branching angle θ, which should be made as small as possible to avoid losses.

When QDs are stamped onto the straight portions of the guide, they downconvert the pump light and radiate photons in all directions with similar probability. QD luminescence that does not propagate in a direction substantially orthogonal to the QD film surface will undergo total internal reflection at the waveguide / cladding interface and couple back into the waveguide. Depending on the refraction indices, more than 80% of the radiation will not escape into air. This process is illustrated in the "Lossy Design" of Figure 1-8.

By employing a photonic crystal structure, we may be able to extract over 90% of the QD emission. A periodic variation at the interface between a thin film dielectric waveguide and the cladding material creates a band gap in the waveguide dispersion such that light frequencies falling within this gap cannot propagate in the guide [41]. By tuning the periodicity, it is possible to align the center of this band gap with the center of the quantum dot emission. QD emission is prohibited from existing within the waveguide and we achieve up to a five-fold extraction efficiency gain. For multiple frequencies needed to achieve white light, we use separated color centers and corrugate different sections of the guide with different periodicities. The periodic variation can be achieved by stamping or nano-imprinting.

DESIGN #2

QD LUMINESCENCE

$n_{QD\ FILM}$

$n_{WAVEGUIDE}$

CORRUGATED WAVEGUIDE

LOSSY DESIGN

QD LUMINESCENCE

WITHOUT WAVEGUIDE CORRUGATION OVER 80% OF QD LUMINESCENCE IS CAPTURED AND GUIDED BY THE WAVEGUIDE
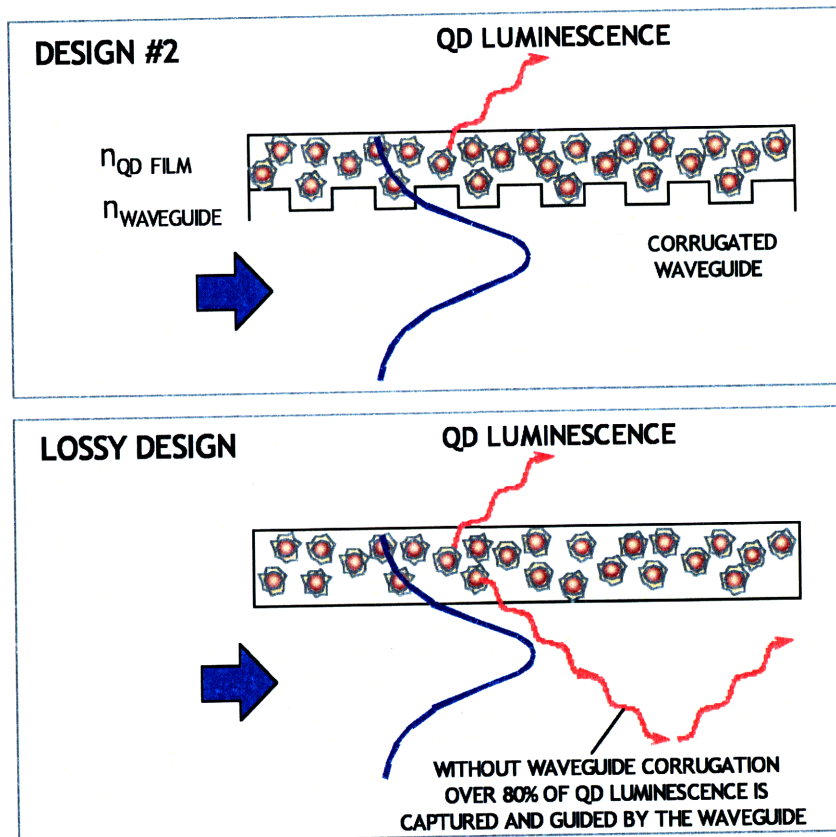
Figure 1-8: A photonic crystal structure will improve light extraction.

Chapter 2

Evanescent Coupling Theory

Our goal is to excite fluorescent material using energy in the evanescent field of a guided mode. The waveguide should be engineered to maximize the intensity of the evanescent field and hence the attenuation due to fluorescence. The geometry should also ensure that all energy-carrying modes are evanescent in the cladding.

The waveguide of interest is a four layer dielectric slab. Our core material is spun onto a quartz substrate and covered with a cladding layer containing quantum dots. The fourth layer is air. Figure 2-1 illustrates this setup.

In this chapter we solve for the mode profile of the guide. Our approach has two parts. First we determine a practical geometry to maximize the attenuation due to fluorescence. Second, we estimate a numerical value for this maximal attenuation.

2.1 Slab Waveguide Analysis

In the ray model of light propagation, a dielectric waveguide is based on the principle of total internal reflection: light with a shallow bouncing angle θ is confined to a core of optically dense material by less dense cladding layers. In a symmetric waveguide, both cladding layers have the same refractive index, and the modes are well known [27, 21, 16]. In our case, however, the cladding layers differ leading to an asymmetric guide. As will be shown, this asymmetry has interesting affects on field confinement.

The slab waveguides are assumed to be infinite in extent such that light is confined

in only one dimension. Practically, this leads to the necessity that $L \gg L_c$, where L_c is the coherence length of light in the guide material. We show in Section 2.1.5 that the effective index method provides the necessary corrections in the case of two-dimensional confinement.

2.1.1 Harmonic Wave Equation in Nonuniform Dielectric

An equation for harmonic solutions of the vector potential $\mathbf{A}$ in a source-free, nonuniform dielectric, $\varepsilon = \varepsilon(\mathbf{r})$, can be found by reducing Maxwell's equations in the standard manner [16].

$$\vec{\nabla}^2 \mathbf{A} + \omega^2 \mu_o \varepsilon \mathbf{A} = \vec{\nabla} \cdot \mathbf{A}$$

Throughout this section, Φ is the scalar potential, ϵ_o is the permittivity of free space, μ_o is the permeability of free space, and ω is the frequency of the radiation. In the Lorentz gauge,[1] where $\vec{\nabla} \cdot \mathbf{A} + j\omega\mu_o\varepsilon\Phi = 0$, the time harmonic wave equation is

$$\vec{\nabla}^2 \mathbf{A} + \omega^2 \mu_o \varepsilon \mathbf{A} = -j\omega\mu_o \vec{\nabla} \left(\varepsilon \Phi \right) \tag{2.1}$$

In uniform dielectrics, the Lorentz gauge decouples the vector potential from the scalar potential. Here the coupling induced by nonuniform ε is weak when the spatial variation of ε is small over a wavelength: $\vec{\nabla} \left(\varepsilon \Phi \right) \approx 0$ Neglecting this coupling entirely reveals a useful approximation for $\mathbf{A}$:

$$\vec{\nabla}^2 \mathbf{A} + \omega^2 \mu_o \varepsilon \mathbf{A} = 0 \tag{2.2}$$

---

[1]The vector potential is not unique. Consider the four vector potential $A \equiv (\Phi, \mathbf{A})$ which satisfies the six independent constraints of Maxwell's equations. Then so does $A'_\mu = A_\mu + \partial_\mu \chi$ where χ is an arbitrary scalar function of $(t, \mathbf{r})$. We are liberty to choose χ to make the problem easier. In this case we use the Lorentz gauge, $\partial_\mu A^\mu = 0$, which is a relativistic extension of the Coulomb gauge, $\nabla \cdot \mathbf{A} = 0$.

The observed fields are recovered through

$$\mathbf{E} = -j\omega\mathbf{A} - \vec{\nabla}\Phi \tag{2.3}$$

$$\mathbf{H} = \frac{1}{\mu_o}\left(\vec{\nabla} \times \mathbf{A}\right) \tag{2.4}$$

We assume that our guide consists of dielectric slabs in the yz-plane, and all variation occurs in the $\hat{x}$ direction: $\varepsilon = \varepsilon(x)$. For an infinite planar interface, there are two classes of incident fields: transverse electric (TE) and transverse magnetic (TM). For the coordinate system shown in Figure 2-1, TE fields satisfy the boundary condition

$$\left.\frac{\partial H_z}{\partial x}\right|_{\mathcal{S}} = 0,$$

where $\partial/\partial x$ is, in general, the normal derivative at a point on the boundary $\mathcal{S}$. In requiring the tangential $\mathbf{H}$ field to be constant at the boundary, we force $E_z = 0$ everywhere. Similarly, TM fields satisfy

$$E_y|_{\mathcal{S}} = 0.$$

This boundary condition implies that $H_z = 0$ everywhere [21]. Given an electric field incident on an interface, $\mathbf{E}$, we can find the magnetic field through Faraday's Law:

$$\nabla \times \mathbf{E} = i\omega\mu\mathbf{H} \tag{2.5}$$

Conversely, given a magnetic field incident on an interface, $\mathbf{H}$, we can find the electric field through Ampere's Law with $\mathbf{J} = 0$:

$$\nabla \times \mathbf{H} = -i\omega\epsilon\mathbf{E} \tag{2.6}$$

For TE modes, $\mathbf{A}$ will be $\hat{y}$ oriented. For TM modes, $\mathbf{A} \cdot \hat{y} = 0$. From these simplifications we can write

$$\mathbf{A} = \hat{e}(x,z)u(x)e^{-j\beta z} \tag{2.7}$$

27

where β is the propagation constant to be solved for. The polarization $\hat{e}(x, z)$ varies between TE and TM modes as just described. The exponential factor contains the entire z dependence so that the remaining factor $u(x)$ is independent of z. The entire solution is invariant under translation in the $\hat{y}$ direction as the slabs are assumed infinite.

We can substitute (2.7) into (2.2) to obtain a wave equation for u:

$$\frac{\partial^2}{\partial x^2} u(x) + \left[\omega^2 \mu_o \varepsilon(x) - \beta^2 \right] u(x) = 0 \tag{2.8}$$

Equation (2.8) has the same form as the time independent Schrödinger equation for a particle in a one-dimensional potential well where $V(x) = -\omega^2 \mu_o \varepsilon(x)$. However, this similarity is mathematical only. The Schrödinger equation is statement of energy conservation between kinetic, potential, and total energy terms. In contrast, (2.8) is a conservation of photon momentum. It also has three terms: transverse and longitudinal momentum, and a location dependent total momentum.[2] The longitudinal momentum of the mode is the square-root of the eigenvalue β^2, the transverse momentum is the square-root of the curvature $-\partial^2/\partial x^2 u(x) \equiv k_x^2(x)$, and the total momentum is the square-root of $\omega^2 \mu_o \varepsilon(x)$, which depends on x. The conservation relation can be visualized as a vector sum, as in Figure 2-1. Bounded solutions exist if and only if the transverse momentum $\omega^2 \mu_o \varepsilon(x) - \beta^2$ is positive only for a local region of x and negative elsewhere [16]. As expected from quantum mechanics, bounded solutions correspond to guided waves and exist only for discrete values of β^2.

The mathematical similarity between (2.8) and the Schrödinger equation is conceptually powerful because it allows us to apply our intuition of potential wells in quantum mechanics to complex optical guides. Here the "potential" profile of interest is $V(x) = -n^2(x)$, where $n^2 = \varepsilon/\varepsilon_o$ is the refractive index of the material. The vacuum potential is -1; it can be shifted to zero by employing susceptibility $\chi = n^2 - 1$ in lieu of refractive index. The "kinetic energy" is the curvature $-(\partial^2 u/\partial x^2)/k^2$, and the total energy is the effective index $N^2 \equiv \beta^2/k^2$ which ranges from V_{min} (com-

---

[2] The total momentum of the photon changes because momentum is transfered between the photon and the dielectric at each interface.
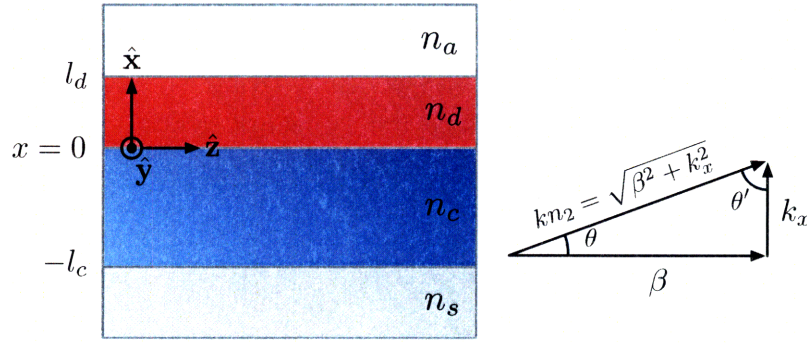
Figure 2-1: Four Layer Slab Dielectric Waveguide. Core material n_c is sandwiched between quantum-dot containing cladding layer n_d and substrate layer n_s. Air, n_a, covers the quantum-dot layer. The slab continues in the $\pm \hat{y}$ direction for $L > L_c$. The free-space wavelength of light is $\lambda = 2\pi/k$, with $k^2 = \omega^2 \mu_o \epsilon_o$.

plete confinement) to -1 (no confinement). We have normalized quantities to k, the vacuum wave vector: $k^2 = \omega^2 \mu_o \varepsilon_o = 2\pi/\lambda$.

2.1.2 Dielectric Profile and Field Construction

Our waveguides have a four layer structure: substrate (s), core (c), quantum-dot cladding (d), and air (a), as in Figure 2-1. Our choice of coordinates is to describe waves guided in the $\hat{z}$ direction and assume translational invariance in the $\hat{y}$ direction. The substrate and air are assumed semi-infinite. Assuming the cladding to be semi-infinite and neglecting the air layer leads to an asymmetric slab dielectric waveguide, which has been solved by Kogelnik and Ramaswamy [26]. This assumption is valid for the lowest order modes. It fails, however, to predict higher mode orders, as will be shown.

Field solutions

We can draw an optical potential for our structure, as in Figure 2-2, and use (2.8), (2.7), and (2.2) to calculate solutions for the vector potential $\mathbf{A}$. As in the quantum mechanical case, the solutions of u are piecewise. If $N = \beta/k > n_d$ then u has the

form

$$
\begin{aligned}
u_s &= A_s e^{\alpha_s x} & x < -l_c \\
u_c &= A_{c+} e^{ik_x^c x} + A_{c-} e^{-ik_x^c x} & -l_c < x < 0 \\
u_d &= A_{d+} e^{ik_x^d x} + A_{d-} e^{-ik_x^d x} & 0 < x < l_d \\
u_a &= A_a e^{-\alpha_a x} & x > l_d
\end{aligned}
\tag{2.9}
$$

and if $N > n_d$ then u is of the form

$$
\begin{aligned}
u_s &= A_s e^{\alpha_s x} & x < -l_c \\
u_c &= A_{c+} e^{ik_x^c x} + A_{c-} e^{-ik_x^c x} & -l_c < x < 0 \\
u_d &= A_{d+} e^{-\alpha_d x} + A_{d-} e^{\alpha_d x} & 0 < x < l_d \\
u_a &= A_a e^{-\alpha_a x} & x > l_d
\end{aligned}
\tag{2.10}
$$

Equations (2.9) and (2.10) satisfy (2.8) if we identify

$$
\begin{aligned}
k_x^{c2} &= k^2 \left(n_c^2 - N^2 \right) \\
k_x^{d2} &= k^2 \left(n_d^2 - N^2 \right) \\
\alpha_s^2 &= k^2 \left(N^2 - n_s^2 \right) \\
\alpha_d^2 &= k^2 \left(N^2 - n_d^2 \right) \\
\alpha_a^2 &= k^2 \left(N^2 - n_a^2 \right)
\end{aligned}
$$

where $k^2 = \omega^2 \mu_o \varepsilon_o = 2\pi/\lambda$ is the vacuum wave vector, and N is the effective index of the mode, for which we will need to solve.

To solve for the coefficients in u, we enforce that u and its first derivative be continuous. After normalizing A_a to unity, we have six equations and six unknowns: N, A_s, $A_{c\pm}$, and $A_{d\pm}$. N^2 is analogous to the energy level E from quantum mechanics.

Impedance matching to find N

In QM, we would grind through the algebra and find all unknowns simultaneously. However, optics affords us a better approach. Using the impedance matching method described by Yuen [50] and Haus [16], we can write down a condition on N indepen-
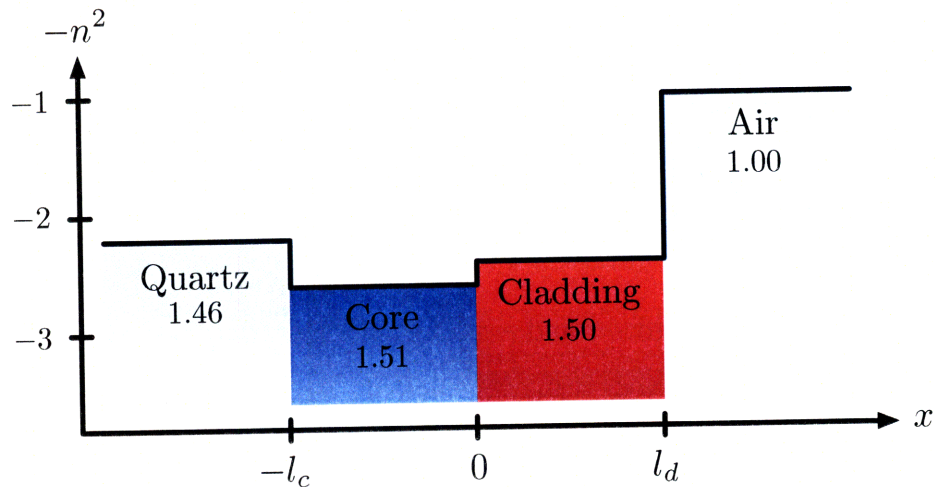
Figure 2-2: Optical potential for the four-layer dielectric waveguide. From Eqn. (2.8), the potential is $V(x) = -\omega^2 \mu_o \epsilon(x)$. As described in the text, (2.8) has been scaled by the vacuum wave-vector $k^2 = \omega^2 \mu_o \epsilon_o$. The scaled potential is plotted here for realistic waveguide parameters.

dent of u.

The characteristic impedance of an optical layer is defined as the ratio of the tangential components of the electric to magnetic field with respect to a propagation direction. Taking the indices i, j, k to represent Cartesian unit vectors, we have:

$$Z_o^{\pm i} \equiv \pm \varepsilon_{ijk} E_j / H_k. \tag{2.11}$$

where ε_{ijk} is the Levi-Civita symbol and $+\hat{\imath}$ means looking towards the $-\hat{\imath}$ direction. The impedance will be purely real if the $\mathbf{E}$ and $\mathbf{H}$ fields are in phase, and purely imaginary when $\mathbf{E}$ and $\mathbf{H}$ are $\pi/2$ out of phase. The power flux is $\mathbf{S} = \mathbf{E} \times \mathbf{H}$. Hence real impedance represents $\hat{\jmath}$ directed energy propagation without attenuation, whereas imaginary impedance represents evanescent decay with zero power flux.

Maxwell's equations for the fields across a dielectric interface require the tangential $\mathbf{E}$ and $\mathbf{H}$ fields be continuous. Indeed, in physical cases it is sufficient to require only that the ratio of the tangential fields be continuous. We see that matching impedances across a boundary is equivalent to matching the Maxwellian boundary conditions.

In our case, we set up the problem for $\hat{x}$ propagating energy and require the

impedance in the cladding layers be imaginary. The characteristic impedance in dielectric layer $j = \{s, c, d, a\}$ is:

$$Z_o^j = \begin{cases} \pm\frac{E_y}{H_z} &= \pm\frac{j\omega\mu_o}{\alpha_x^j} & \text{for TE modes} \\ \mp\frac{E_y}{H_z} &= \pm\frac{\alpha_x^j}{j\omega\epsilon_j} & \text{for TM modes} \end{cases} \qquad (2.12)$$

where $+$ means looking toward $-\hat{x}$ and $-$ means looking toward $+\hat{x}$. α_x^j is the transverse wave-vector, defined as $\alpha_x^j = k\sqrt{N^2 - n_j^2}$. α_x is imaginary for core materials and real for cladding materials so that the impedance is real for layers that propagate energy and imaginary for evanescent decay.

The impedance is transformed over a distance Δx through material Z_o^j by:

$$Z(x = x_o + \Delta x) = Z_o^j \frac{Z(x_o) + Z_o^j \tanh(\alpha_x^j \Delta x)}{Z_o^j + Z(x_o) \tanh(\alpha_x^j \Delta x)} \qquad (2.13)$$

The impedance at the first boundary, $x = -l_c$, is the impedance of the substrate, Z_o^s. Thus $Z(-l_c) = Z_o^s$. This impedance is transformed by the core layer to be

$$Z(0) = Z_o^c \frac{Z(-l_c) + Z_o^c \tanh(\alpha_x^c l_c)}{Z_o^c + Z(-l_c) \tanh(\alpha_x^c l_c)}$$

at the core / qd-cladding interface. The cladding transforms $Z(0)$ into

$$Z(l_d) = Z_o^d \frac{Z(0) + Z_o^d \tanh(\alpha_x^d l_d)}{Z_o^d + Z(0) \tanh(\alpha_x^d l_d)}$$

at the cladding / air interface. For impedances to match and boundary conditions met, this impedance must equal the impedance of the air as seen from the guide. Thus

$$Z(l_d) = -Z_o^a \qquad (2.14)$$

the negative sign appearing because we look in the $+\hat{x}$ at the air impedance. Equation (2.14) is our propagation condition. Only values of N that self-consistently match impedances create propagating modes.

32

2.1.3 TE Solutions

Using MATLAB, we can write a script to plot functions of the TE solutions. As indicated by (2.10) and (2.9), there are two classes of solutions. When $N > n_d$, the propagation is confined to the core the is evanescent in the quantum dot cladding. When $N < n_d$, the modes are carried by both the core and quantum dot cladding layers. We wish to avoid the second as it would not be evanescent-coupling.

Figure 2-3 shows solutions for some waveguide geometries. In the first configuration, the cladding and dot layer are each one wavelength thick with a $\Delta n = n_c - n_d = 0.1$. For this configuration, there are no modes that are contained to only the core material because $N < n_d$ for both guided modes. We can change the waveguide geometry to accommodate a mode that is confined to the core, i.e. $N > n_d$. In the second configuration, the change is to expand the core width to 3λ. In the third configuration, we increase Δn to 0.3. Each of these modifications decreases the energy of the first mode to fix into the core well. However, modes are still allowed that propagate in both the core and cladding. Clearly the geometry needs to be carefully considered to have all allowed modes be evanescent in the cladding layer.

We can also try something clever where we switch the dot and core layers. The idea here is that we put the core next to the air layer and the dots next to the substrate. The different optical potential may give more advantageous modal profiles. However, this change is seen to increase the asymmetry of cladding sandwiching the core. As will be shown in Section 2.1.4, increasing asymmetry increases the cutoff and only exacerbates the situation.

The locus of solutions to the four layer guide can be visualized on a normalized dispersion diagrams, shown in Figure 2-4. Recognizing that the index of the substrate and air are fixed, we can normalize solutions to the index of the core and the index of the QD cladding layer.

$$N \to N' = \sqrt{\frac{N^2 - n_s^2}{n_c^2 - n_s^2}} \tag{2.15}$$

The normalization can be understood as follows. The nominal dispersion is ω versus N—i.e., how changing the frequency of incoming light changes the mode wavevec-

a	sub	core	dots	air
n	1.46	1.51	1.50	1
l	–	λ	λ	–

b	sub	core	dots	air
n	1.46	1.51	1.50	1
l	–	3λ	λ	–

c	sub	core	dots	air
n	1.46	1.53	1.50	1
l	–	λ	λ	–
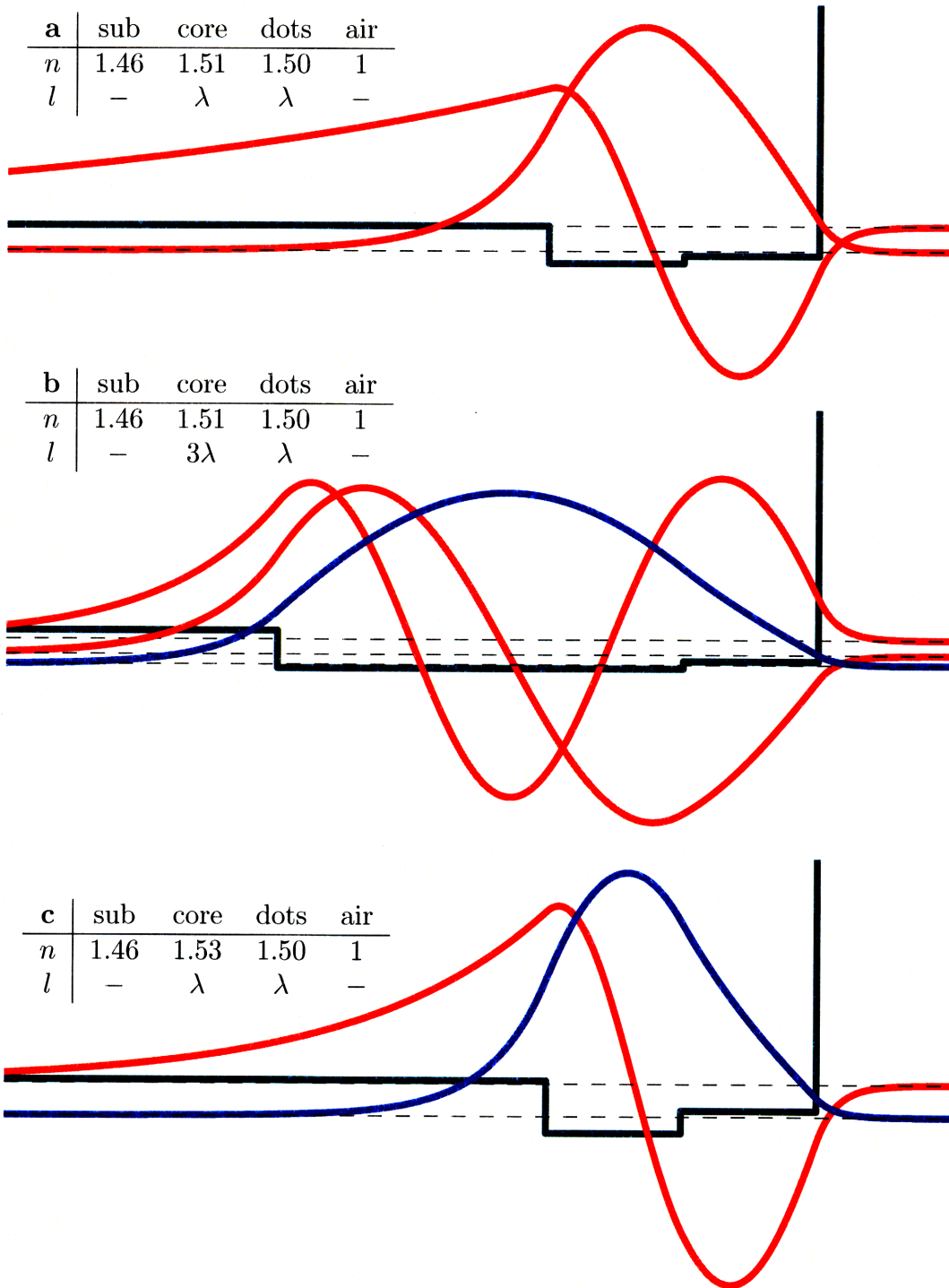
Figure 2-3: TE solutions for selected waveguide geometries. Green lines represent the optical potential and black lines show the energies of the modes relative to the potential. For a mode to be confined to the core, we require that the modal energy fall below the cladding energy; these desirable modes evanescent in the cladding are plotted in blue. The first geometry permits no cladding-evanescent solutions. Changing the geometry $l_c \rightarrow 3l_c$ or $\Delta n \rightarrow 3\Delta n$ allows cladding-evanescent modes.

tor, β, and $\beta/k = N$—for a specified waveguide geometry. In our exploration, we know the frequency of guided light: it is our 3 eV excitation. So we would rather plot solutions for varying waveguide geometries versus N. Assuming that the substrate and air have fixed indices, the independent variables are n_c, n_d, l_c, and l_d.

Our idea was predicated on avoiding thick or concentrated films of fluorescent materials; whatever l_d is, it is much smaller than a wavelength. It would be most informative to plot N versus l_c, as we are curious about how changing l_c changes the number of guided modes, etc.

We could naïvely plot N versus l_d for several n_d, n_c, and small l_d and look for a pattern. However physical meaning motivates the normalization. N is the modal "energy", which, for a guided mode, will fall between n_s and n_c: $n_s < N < n_c$. For $n_c > N > n_d$ the mode will be guided only in the core; for $n_s < N < n_d$ the mode is guided by both the core and the dot cladding. Our normalization changes the range of the y axis from $[n_s \; n_c]$ to $[0 \; 1]$. The scaling is performed in quadrature in accordance with our optical potential energy scale, $V \propto -n^2$. Finally we choose to plot N'^2 instead of N' because this scale gives greater resolution for high values of N.

Figure 2-4 plots dispersion diagrams for increasing values of l_d as a function of l_c for the first five modes. A fifth plot shows the dispersion limits as $l_d \to 0$ and $l_d \to \infty$; these limits correspond to three layer structures discussed below. We discover the following:

- As l_d increases, the fundamental mode cutoff disappears. Practically this means that the fundamental mode will always propagate. Unfortunately this mode will not be evanescent in the cladding.

- For $n_c \sim n_d$, there are no geometries for single mode propagation where all modes are confined to the core. The only way to design a single mode guide where the single mode is confined only to the core is to increase the index difference between the core and the QD cladding, such that $n_d'^2 \approx 0.5$

- The lowest order modes of multimode guides (l_c large) will be evanescent in the cladding, but the higher order modes will not.
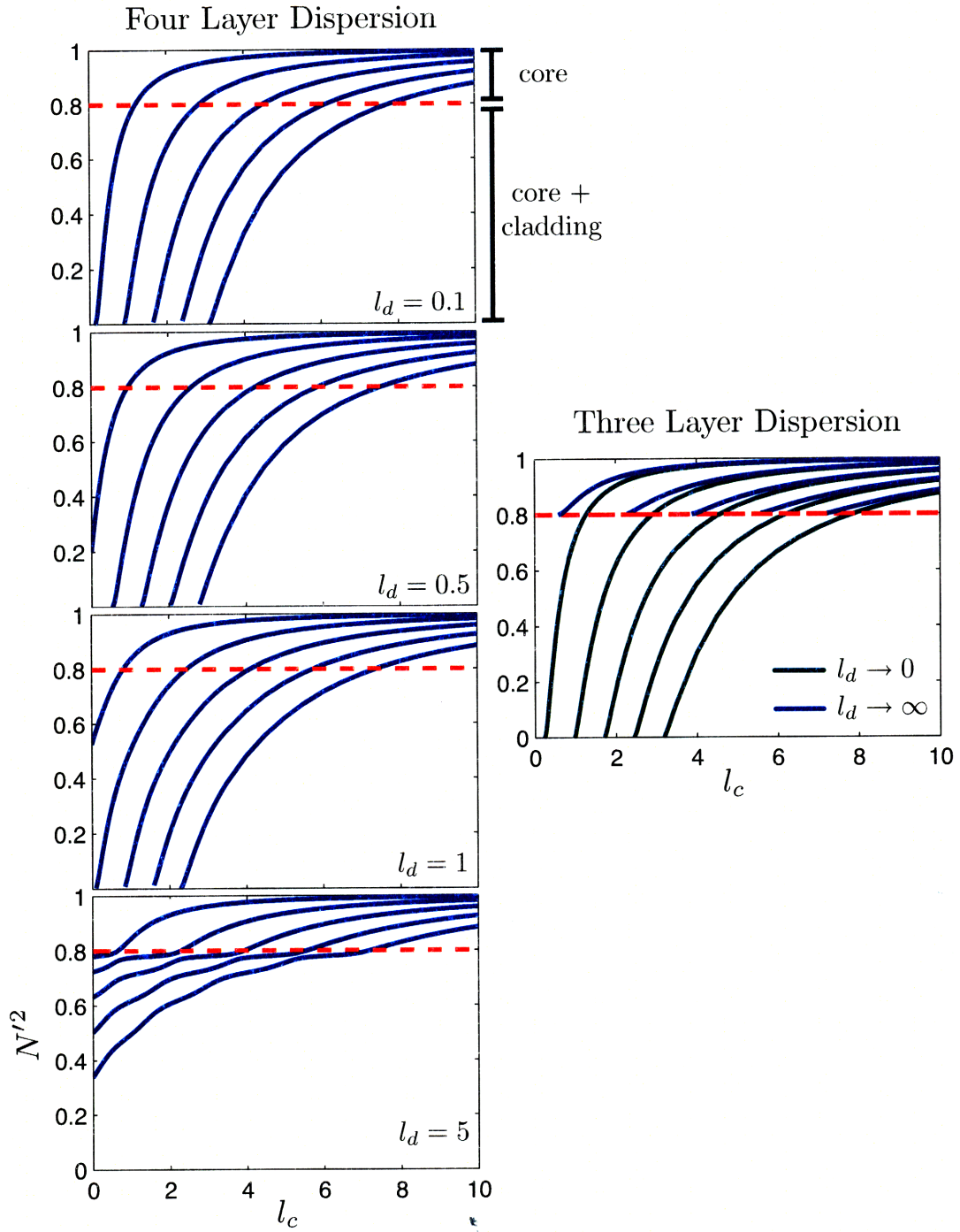
Figure 2-4: Normalized dispersion diagrams for various four layer geometries showing the first five modes. The red line represents the index of the QD layer. Modes with $N'^2 > 0.8$ are confined to the core with cladding-evanescence; modes with $N'^2 < 0.8$ are guided in both the core and cladding. For $n_d \sim n_c$, there are no configurations for single mode propagation where the single mode is confined to the core. Further discussion appears in text.

2.1.4 Three Layer Approximation

When the modes are confined to the core ($N > n_d$) and we have a thick QD cladding layer ($l_d \gg 1/\alpha_d$), we can neglect the air and approximate the guide as a three layer structure. The advantage is that the three layer structure can be normalized to the quantity $n_c{}^2 - n_d{}^2$. This normalization allows us to gain insight without focusing on specific guide characteristics.

From [26] we are guided to identify the normalized guide index as

$$N'^2_{\text{TE}} \equiv (N^2 - n_d{}^2)/(n_c{}^2 - n_d{}^2) \qquad (2.16)$$

which varies between zero and unity for $n_d \geq n_s$. The zero represents the cutoff condition, $\theta' > \theta_c$, where $N = n_d$. Unity occurs for $\theta = 0$ where $N = n_s$. The inversion of Equation 2.16 to recover N from N'^2 is:

$$N^2 = n_s{}^2 + N'^2 \left(n_c{}^2 - n_d{}^2 \right) \qquad (2.17)$$

We also introduce the normalized frequency

$$V \equiv kd\sqrt{n_c{}^2 - n_d{}^2} \qquad (2.18)$$

and the asymmetry parameter, a, as

$$a_{\text{TE}} \equiv (n_d{}^2 - n_s{}^2)/(n_c{}^2 - n_d{}^2). \qquad (2.19)$$

The measure a can range from zero for a symmetric guide ($a = 0$ if $n_s = n_d$) to infinity for strong asymmetry ($a \to \infty$ if $n_d \neq n_s$ and $n_d \to n_c$).

The solution locus for N'^2 in the three layer approximation is plotted in Figure 2-5. We observe the following. In the symmetric limit, $a \to 0$, the TE $m = 0$ mode is always guided. However, for $a > 0$, there is a cutoff frequency for the lowest order mode, $V_c = \tan^{-1}\sqrt{a}$. In the limit $a \to \infty$, $V_c = \pi/2$. A cutoff for the lowest order mode is unique to asymmetric guides.

Solution locus for TE modes of asymmetric waveguide

Axis labels:
- y-axis: N'^2 (normalized N)
- x-axis: $V = kd\sqrt{n_c^2 - n_d^2}$ (normalized ω)

Curve labels: $m = 0$, $m = 1$, $m = 2$, $a = 0$, $a = 1$, $a = \infty$
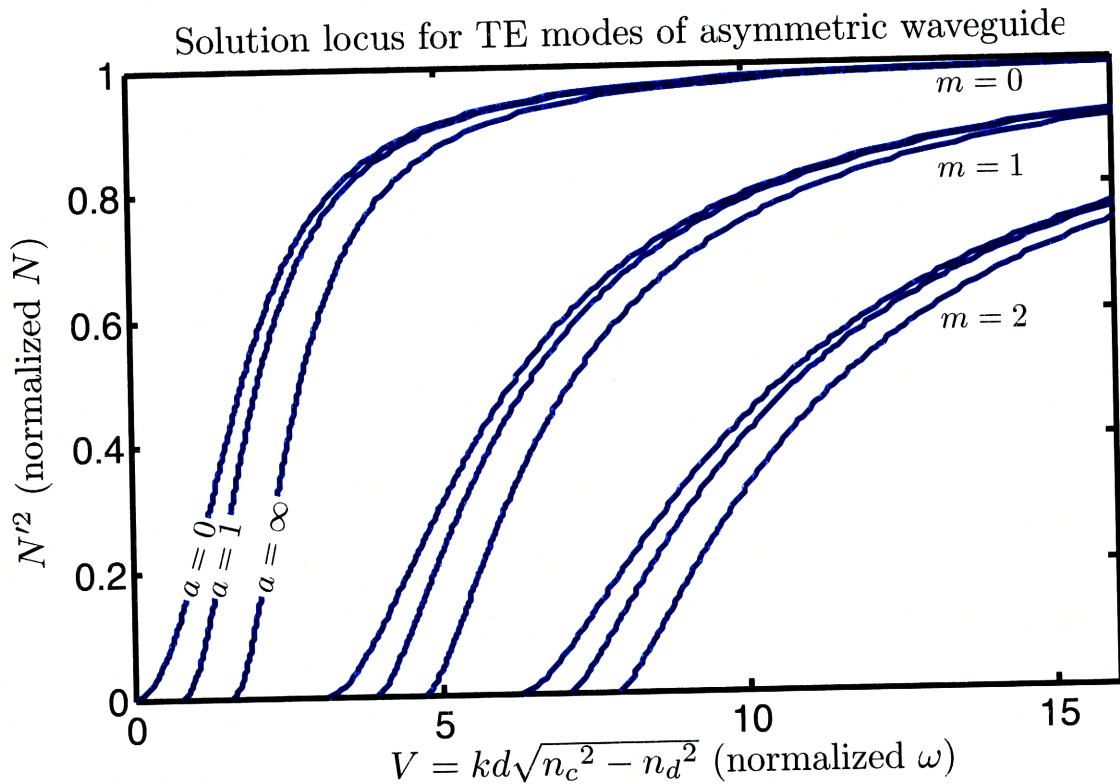
Figure 2-5: TE Solution Locus for Asymmetric Slab Waveguide parameterized by asymmetry parameter a and mode number m. Light with frequency ω (normalized to V through Equation 2.18) will be guided with propagation constant N (normalized to N' with Equation 2.16). In the symmetric limit, the asymmetry parameter a drops to zero and the lowest order mode $m = 0$ is always guided (Equation 2.19). For $a > 0$, a guided mode is not guaranteed.

2.1.5 Effective Index Method

Using the effective index method of K. S. Chiang, we can adjust our calculations above to account for y confinement of modes [8, 9, 10]. The adjustment is a small correction to the refractive index of each layer based on the index of the confining dielectric. For wide waveguides, $L \gg L_c$, we ignore this correction.

2.2 Optimal Geometry

Having solved for the fields of the waveguide, we can now evaluate the optimal geometry. We search for modes evanescent in the cladding; of these modes, the metric of interest is the percentage of the mode intensity that lies in the cladding.

From Equation 2.10, we know that an evanescent field in the cladding will go as $E = e^{-\alpha x}$. In a quantum potential well, $E = \hbar^2 k^2 / 2m$, and

$$\alpha = \sqrt{\frac{2m(V - E)}{\hbar^2}}$$

By analogy, $V = -n_d^2$ and $E = -N^2$; an evanescent field in the QD cladding will attenuate with

$$\alpha \sim \sqrt{N^2 - n_d^2}. \tag{2.20}$$

Furthermore, the energy density increases with square of the field. Thus the intensity contained in the cladding is, in the trapezoidal approximation:

$$\mathcal{I} \propto \frac{1}{l_d} \int_0^{l_d} e^{-2\alpha x} \, dx \approx 1 - 2\alpha l_d \tag{2.21}$$

We see that we want a small alpha for high cladding intensities.

We divide the solution space between single mode, multi-mode, and massive guides. We will conclude that, with flat illumination, a singlemode guide is the best for our application.

2.2.1 Single Mode Guides

We want a single mode waveguide that

- allows only one mode evanescent in the cladding ($N > n_d$), and

- has a high cladding intensity (equivalently, a small $\alpha \sim \sqrt{N^2 - n_d{}^2}$).

Examining the solution curves for the four layer structure in Figure 2-4, we look for single mode solutions. These are solutions for which l_c is small and a vertical line from the l_c axis intersects only one blue mode-dispersion line, indicating that for that frequency there is only one solution for N. For the $l_d = 5\lambda$ solution set, even at $l_c = 0$ there are many allowed modes. Only five are plotted, but it appears that up eight modes might propagate at $l_c = 0$. So we want a small l_d.

We also want the single mode to be confined the core. In terms of the figure, we want the intersection to occur above the red line. In the $l_d = 0.1\lambda$, the range of l_c which gives a single mode guide (approximately $0 < l_c < 0.5\lambda$) has no solutions above the red line. Clearly we must move the red line down to realize a single mode guide confined to the core. Decreasing the red line is equivalent to adjusting the index of the dot cladding layer to be closer to the substrate index or increasing the index of the core. From the figure, we need the red line to fall at 0.5 or below. Then we will have a small range of l_c that give single mode guides where the mode is evanescent in the cladding. The mode that results is shown in Figure 2-6(a).

Let's check what happened to alpha when we moved the red line. We have either increased the index of the core or decreased the index of the dot cladding. These changes are roughly equivalent. In turn, N also changes. It is unclear from this analysis how alpha changed: $\alpha^2 = N^2 - n_d{}^2$. However, we can perform simulations to get a clearer picture. These show that as we move the red line lower, the cladding intensity increases for the fundamental mode. So the change in N' must outpace the change in n_d'.

We conclude that for a single mode waveguide to be evanescent in the cladding, the thickness of both the core and cladding must be small and the index contrast

between the core and cladding must be large. Conveniently, this combination leads to a high cladding intensity.

2.2.2 Multimode Mode Guides

We can also consider a multimode guide, where $0.1\lambda < l_c \ll L_c$, where L_c is the coherence length of our waveguide. For polymer guide, the coherence length is between 12 and 50 microns [2, 23, 22]. We still disregard thick quantum dot layers because we wish to avoid reabsorption of emitted light.

Consider the dispersion plot $l_d = 0.1\lambda$ in Figure 2-4 at the point where $l_c = 10\lambda$. We will have many guided modes (only the first five are plotted in the figure). Roughly half of the modes (the lower half) will be evanescent in the cladding, and the upper half will guide in the core and cladding. The exact modes are shown in Figure 2-6(b).

The pertinent question is the energy distribution among the modes. From [39] we know that illumination is approximately flat. The transform is a sinc function and the lowest order mode carries a significant fraction of the total energy [38]. The field coefficient coupling into higher order modes falls off with $1/m$ where m is the mode number; the energy falls off as $1/m^2$. For flat illumination, we are able to ignore higher order modes entirely! Hence in a multimode guide, the energy is, for all practical purposes, confined to the core. Furthermore, a wide range of l_c and l_d are acceptable.

However, when we examine the cladding intensity, the numbers are unimpressive. Only 0.01% of the fundamental mode energy propagates in the cladding. The attenuation due to dots will be very small.

2.2.3 Massive Guides

Coherence length of polymer waveguides is between 12 and 50 microns [2, 23, 22]. A massive guide is one for which the mode is not coherent; scattering dephases the transverse wavevetor and invalidates the impedance matching conditions. We cannot model this situation, but assume that a multimode guide would be just as good as

41

a	sub	core	dots	air
n	1.46	1.55	1.47	1
l	—	0.5λ	0.1λ	—

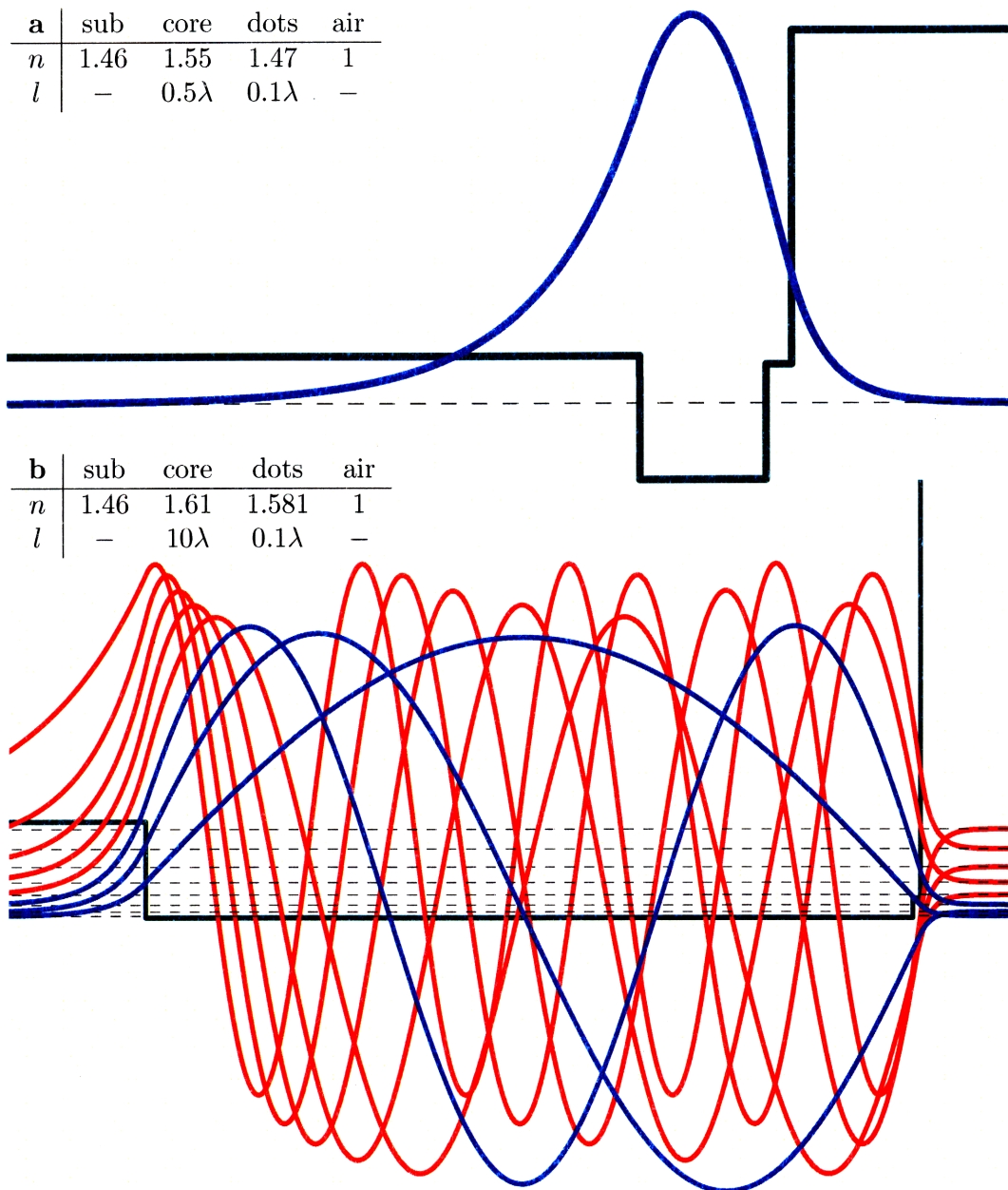| **b**	sub	core	dots	air
n	1.46	1.61	1.581	1
l	—	10λ	0.1λ	—

Figure 2-6: Modes for single and multimode guides evanescent in the cladding. The percentage of energy in the cladding is 3.9% for the single mode and 0.01, 0.02, 0.05, 0.09, 0.14, 0.20, 0.26, 0.32, for modes 0, 1, 2, etc., of the multimode guide.
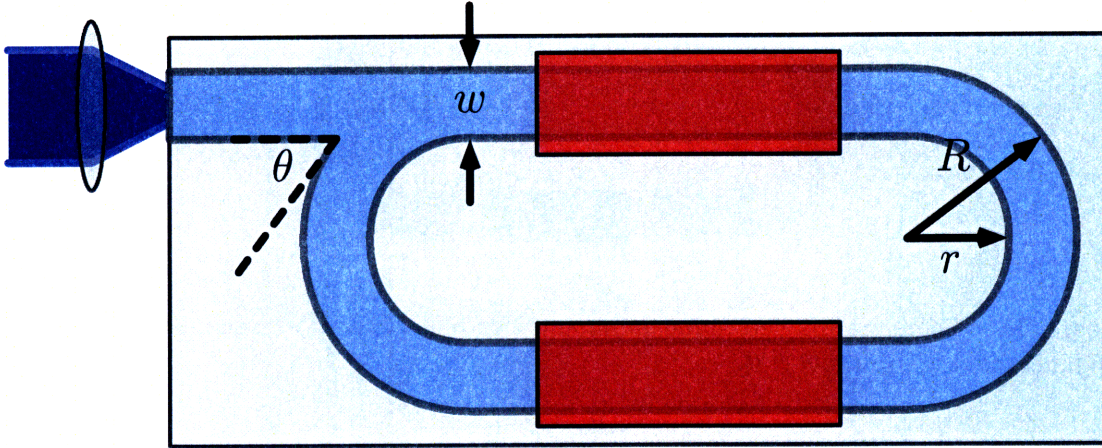
Figure 2-7: Q-shaped waveguide. Marked are critical dimensions and a lens-coupled excitation source.

a massive guide. On the other hand, the low intrinsic losses of massive guides are attractive. Yoshimura reports that a 40 micron square guide has losses of 0.02 dB/cm at 830 nm [49].

2.2.4   Optimal Guide

With flat illumination, a single mode guide is the best for our application. It has a high cladding intensity, yet remains evanescent for the proper selection of indices. We need a high index core and a QD cladding layer with index approximately the same as the substrate.

2.3   Q-Shaped Waveguide

Our Q-shaped waveguide (Figure 2-7) is not unique in integrated optics. For instance, Bradander, *et. al.* use a similar design as a pressure sensor [12]. In contrast to their application, we do not expect coherent propagation around the loop because of the low coherence length of our materials. This quality is advantageous: we also do not worry about destructive interference (which would require us to size the circumference to be an integral number of wavelengths). The two quantities we must consider are
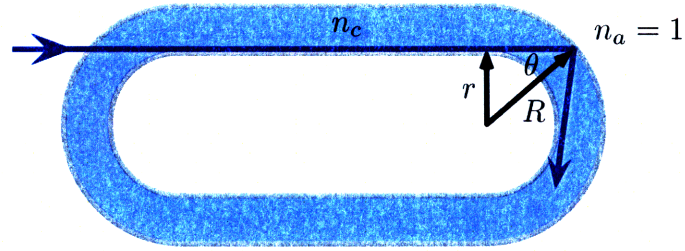
Figure 2-8: Geometry to determine minimum bending radius for q-shaped guide. For guidance, we require the $\theta > \theta_c$.

the bend radius and the branching angle.

Figure 2-8 illustrates the geometry for total internal reflection of guided light around the bend. We require that $\theta > \theta_c$. The ray with minimum θ is shown in picture; satisfying the constraint for this ray will satisfy the constraint for all other rays. From the figure it is clear that $\sin \theta = r/R$. From Snell's law, we determine that $\sin \theta_c = n_a/n_c = 1/n_c$. Thus the radii R and r must satisfy:

$$r > Rn_c \tag{2.22}$$

A realistic outer diameter for our guide is 1 cm, so $R = 5$ mm, and $n_c \approx 1.5$. We find $r > 7.5$ mm, which is satisfied for guides less than 2.5 mm in width. These numbers demonstrate that we can easily meet this bending constraint.

The branching angle, θ in Figure 2-7, should be a small as possible to make the branching an adiabatic change [33, 4]. The steeper the branching angle, the more the recycled light will couple to both forward and backward modes of the Y split. Pratically speaking, we want $\theta < 10°$. We do not explore this consideration quantitatively because it is clear that we can minimize the loss to an arbitrary level by lowering the branching angle.

44

2.4 Periodic Structure for Improved Light Extraction

When QDs are stamped onto the straight portions of the guide, they downconvert the pump light and radiate photons in all directions with similar probability. QD luminescence that does not propagate in a direction substantially orthogonal to the QD film surface will undergo total internal reflection at the waveguide / cladding interface and couple back into the waveguide. Depending on the refraction indices, more than 80% of the radiation will not escape into air. By employing a photonic crystal structure, we may be able to extract over 90% of the QD emission.

We initially proposed using a distributed feedback structure, as discussed in [41]. Periodic corrugation at the core/cladding interface creates a bandgap in the allowed propagation frequencies. The rational is that much of the emitted light will couple into the guide where it will be attenuated through non-emissive mechanisms. If the bandgap were positioned around the emission frequency, any trapped emission would subsequently scatter out of the guide per the bandgap condition.

However, closer examination of the distributed feedback structure reveals that the bandgap is a reflection gap, not a scattering gap. Frequencies incident on the grating would be reflected within the guide, not scattered out of it. As the project progresses, it will be necessary to employ a more intricate photonic crystal structure that will scatter emission frequencies instead of reflecting them.

Chapter 3

Quantum Dot Chemistry

Quantum dots (QDs) are the subject of intense research for their promising applications to quantum optics, nano-electronics, medical imaging, and visual displays. Of these areas, QD luminescence is certainly the most visually compelling. This thesis focuses specifically on photoluminescence (versus electroluminescence). Photoluminescence from QDs is particularly attractive because absorption below the band-gap is nearly complete. Thus we can excite a diverse populations of QDs with a single UV light source.

3.1 Theory

We briefly survey the physics of quantum dots, with focus on their optical characteristics.

3.1.1 Chemical Structure

The basic structure of a QD is shown in Figure 3-1. The dot is divided into three parts: the electrically active core, an isolating shell, and chemically active surface ligands. For CdSe, the core ranges between 150 Å and 17 Å for 700 and 410 nm dots, respectively. The large cores have 10^5 unit cells, but the small cores have only 185 unit cells (740 atoms)!
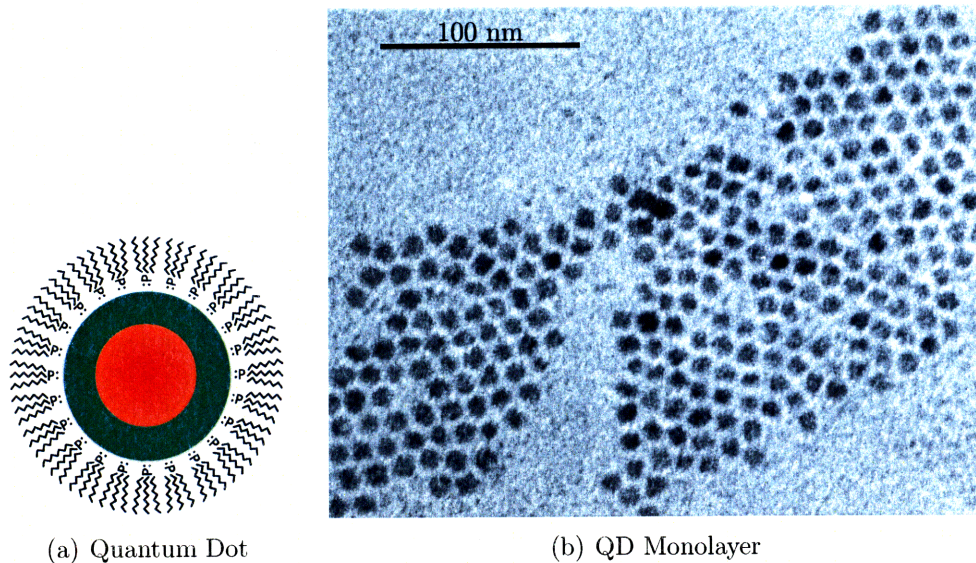
47

(a) Quantum Dot   (b) QD Monolayer

Figure 3-1: Quantum Dot Structure. A quantum dot consists of three parts: an electrically active core, an isolating shell, and chemically active surface ligands. SEM by J. Halpert.

As an illustrative example, take an active core of ZnCdS, which we overcoat with ZnS to improve the electronic isolation of the core. We denote the chemical composition of this dot with the notation (ZnCdS)ZnS. The surface ligands are alkyl-pnictides whose exact formulation is largely dependent on the solvent used during synthesis. Triocytlphosphine (TOP), as shown in Figure 3-1 and its oxide is common.

3.1.2 Electronic and Optical Characteristics

Electrically, a quantum dot is a structure in which a high potential confines the charge carries in three spatial dimensions. Contrast this arrangement with a large piece of metal (bulk material) in which electrons move freely in all directions. This confinement leads to the main attractive features of nanocrystals, as outlined in this section.

Tunable Bandgap

A tunable bandgap is the salient feature of QDs. Unlike in bulk material where the band gap is completely determined by the choice of elements and perhaps crystal

Table 3.1: Roots of spherical Bessel function $j_\ell(x) = 0$.

n/l	1	2	3
1	π	4.493	5.763
2	2π	7.725	9.095
3	3π	10.904	12.323

structure, the nanocrystal band gap varies with the size of the structure. Specifically, as the radius of the dot decreases, there is an additive confinement term to its base band gap proportional to $1/a^2$. Here a is the radius of the dot.

We can model an isolated QD as spherical infinite potential well. An electron or hole placed individually into the well has discrete energy levels [13]

$$E_{l,n}^{e/h}(a) = \frac{\hbar^2 \phi_{\ell,n}^2}{2m_{e/h} a^2} \tag{3.1}$$

indexed by energy level n and angular momentum number l. Here $\phi_{\ell,n}$ is the nth root of the spherical Bessel function of order ℓ, i.e. solutions to the equation $j_\ell(\phi_{\ell,n}) = 0$ (see Table 3.1). The energy levels scale with the effective mass, m, of the electron and holes in the material. Most importantly we see that the energy levels scale with the inverse radius squared. The energy of the lowest electron and hole levels increase with decreasing nanocrystal. The effect is an increase in the energy of the band edge optical transition.

When an electron and a hole occupy the well simultaneously (as in the case of an exciton), we must consider an additional potential term due to the Coulomb interaction,

$$V(a) \propto -e^2/\kappa a, \tag{3.2}$$

where κ is the index of the material. We observe that while quantization energy grows as $1/a^2$, the Coulomb energy grows only as $1/a$. For small dots where a is much smaller than the bulk exciton radius a_B, the Coulomb energy is a small correction term.

For small QDs, we add (3.1) and (3.2) as correction terms to the bulk bandgap.

The absorption peaks are given by [13]

$$\hbar\omega = E_g + E^h(a) + E^e(a) - 1.8\frac{e^2}{\kappa a}. \tag{3.3}$$

The factor of 1.8 has been determined by perturbation theory. These peaks can been seen graphically in Figure 3-2.

QDs as Artificial Atoms

We typically fabricate QDs as type II-VI semiconductor nanocrystals, such as CdS or CdSe. Take CdSe, a wurtzite semiconductor, as an example. Figure 3-3 shows the band diagram for bulk CdSe as calculated in the tight-binding, linear combination of atomic orbitals approximation. The diagram follows from work done by Kobayshi, *et. al.* [25] and Xu, *et. al.* [48]. We see that the heavy hole is approximately 20 times heavier than the electron. When an electron is promoted, an exciton will form. The heavy hole is approximately stationary and the light hole will orbit similar to a hydrogen atom. For this reason, QDs are sometimes called "artificial atoms."

Absorption of CdSe dots is shown in Figure 3-2. In the atomic approximation, the first absorption feature is the $1s$ orbital, the second absorption is $2s$, and so on. Features become blurred by the Rayleigh scattering envelope which increases as $1/\lambda^4$.

This model suggests that the emission spectra of a dot should be like that of hydrogen, with many spectral lines in the visible. However, we only observe radiation from the $1s$ to ground transition. These results are explained by the relative relaxation rates of the different states, where intraband (e.g. $2p \rightarrow 1s$) transitions occur much more rapidly than, say, $2p$ to ground. Hence an exciton always decays to the $1s$ state before recombining, and the dot emission is at the energy of the absorption edge. (QD Stoke shift is negligible.)

Then what about the intraband transitions: where are those photons? From Equation 3.1 and Table 3.1, it is seen that intraband transition energies are a fraction of the $1s$ exciton recombination energy. These energies will be in the far-infrared for CdSe dots.
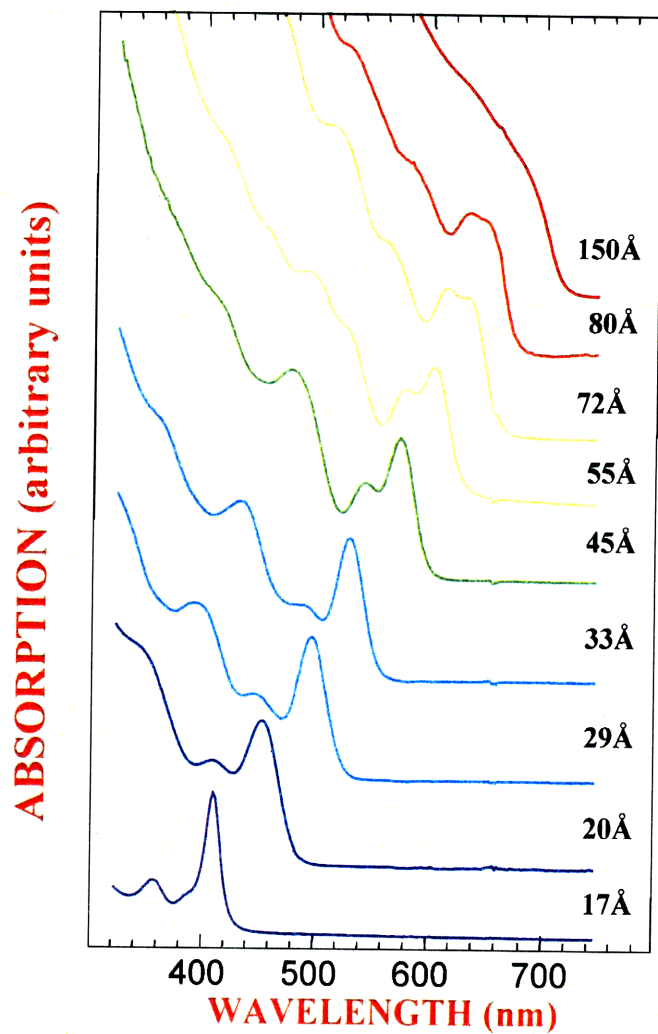
Figure 3-2: Absorption of CdSe quantum dots from C.B. Murray [31]. The absorption band edge blue-shifts from the bulk bandgap of 1.8eV as crystal size decreases. There is a $1/\lambda^4$ envelope from Rayleigh scattering (see Section 4.1.1), although dot absorption does increase with photon energy.
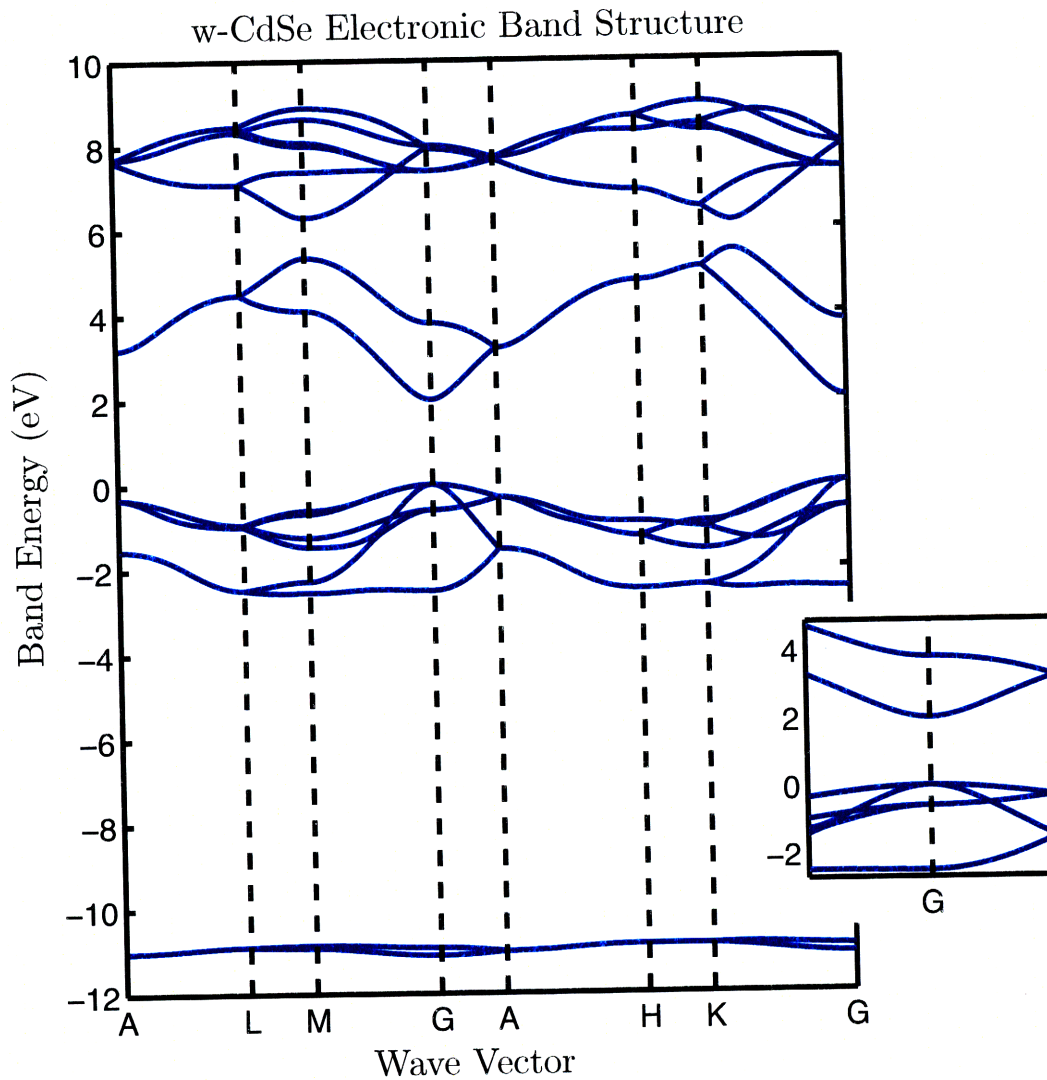
Figure 3-3: Simulated electronic band structure of w-CdSe. From experiment [1], the direct bandgap is 1.8 eV at the Γ point. Averaging over **k** directions, there are two hole masses and one electron mass, measured to be approximately $1.7m_e$, $0.2m_e$, and $0.1m_e$, respectively. Because the mass of the heavy hole is much larger than the mass of the electron, the CdSe exciton is approximately hydrogenic. For this reason, QDs are sometimes called "artificial atoms."

:P

Figure 3-4: Chemical structure of trioctylphosphine. The unpaired electrons on the phosphorous atom passivate the surface of quantum dots.

Surface Chemistry

Because of the large surface area to volume ratio, the surface structure of the crystals play an important role in the electronic structure. Without surface passivation, each dot would have a different Hamiltonian depending on the configuration of the surface anions and cations.

Early dots were passivated by alkyl-pnictides surface ligands such as trioctylphosphine (Figure 3-4). The unpaired electrons attach to the semiconductor surface and present a wall of negative charge that "smooths" out surface details. The electronic properties of the dots are dependent on the stability of these ligands. These capping groups resulted in quantum yields of 10%. It was later found that alkyl-amines were better passivation ligands, and the quantum yields were increased to 50% [5].

More recently the core material of a dot is overcoated with an additional layer of semiconductor whose bandgap sandwiches that of the core. The overcoat performs the same function as organic ligands in electronically passivating the surface of the core. Surface ligands are then attached to the outer layer. The advantage of overcoating is two fold. First, the absorption cross section increases as the now the overcoating material can absorb and inject electrons and holes into the core. Secondly, the overcoating material is less fragile than ligands.

The surface of dots can be functionalized with different groups to allow the dots to react in different systems. For instance, dots can be stabilized in a sol-gel matrix by cap-exchanging the native TOP ligands with aminopentanol.

Table 3.2: Abbreviations of chemicals commonly used in QD synthesis reactions.

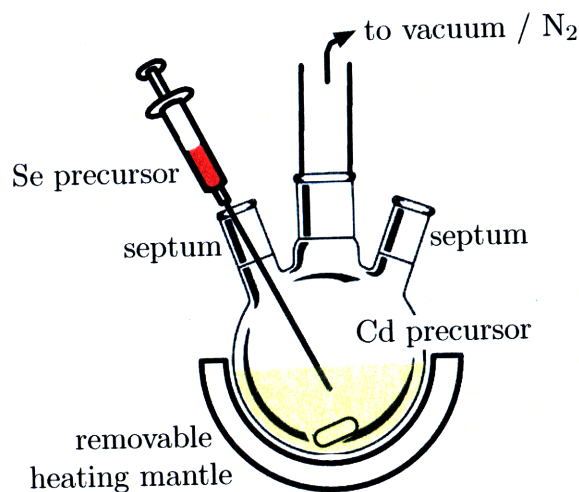|		
TOP	trioctylphosphine	liquid
TOPO	trioctylphosphine oxide	solid
DDA	2,'3'-dideoxyadenosine	liquid
HDA	hydroxy-decanoic acid	solid
Cd(acac)$_2$	cadmium acetylacetonate	solid
TOPSe	trioctylphosphine-selenium	soln
DMS	dimethyl sulfide	liquid
DEZ	diethylzinc	liquid

Figure 3-5: Synthesis for dots.

3.2 Synthesis

There are two steps to the synthesis process of quantum dots. The cores are first precipitated from solutions of organometallic precursors. Next the cores are over-coated with a passivating shell. The entire process takes approximately eight hours. In this section we describe the synthesis of (CdSe)ZnS quantum dots. Abbreviations for chemicals used in synthesis are listed in Table 3.2.

3.2.1 CdSe Core Synthesis

1. Combine 6.25g of 90% TOPO, 5.75g of 98% HDA, and 3.4mL of TOP into a glass pot. These are degassed at 130 °C for 2 hours. After 30 minutes the solution turns a pale yellow.

2. Combine 7.5mL of TOP, 0.5ML DDA, and 317mg of $Cd(acac)_2$ into a vial. Degas at 100 °C for 1 hour. After 15 minutes the solution turns pale yellow.

3. Obtain 2mL of 1.5M TOPSe

4. After degassing finishes, remove vial from heat and allow it to return to room temperature over nitrogen. Put pot over nitrogen and increase heat to 360 °C.

5. When vial reaches room temperature, add TOPSe (still under nitrogen). Draw vial contents into 10mL syringe.

6. This final step precipitates the dots. When the pot reaches 360 °C, in quick sequence remove the insulation and heating mantle, and inject vial contents from 10mL syringe as quickly as possible.

7. Anneal solution at 80 °C for 1 hour.

3.2.2 ZnS Overcoat

Before overcoating, we need to "clean" the cores. The cores are dissolved in TOPO with TOP ligands. The TOPO has a melting temperature of 50 °C, and we add hexane before removing the heat to retain the liquid form at room temperature.

The dots can be "crashed out" of the growth solution by adding a small polar solvent, such as methanol. The dots fall out of solution because they do not dissolve in the methanol. In addition to methanol, it is also necessary to add a bit of butanol as a mediator between the hexane and methanol, which would otherwise not mix.

Crashed dots are centrifuged between 3000 and 4000 rpm for 3 to 5 minutes. The supernatant is discarded. The dots are re-dispersed in hexane, and the crash out procedure is repeated once more.

The overcoating procedure is then dependent on the number and radius of the cores to be overcoated. From the absorption spectra, one can find both the concentration and dot radius. We then measure out the appropriate amounts of DEZ and DMS into TOP so that we will add a 3 to 5 layers of ZnS to the cores.

Using a syringe pump, we slowly add the zinc and sulfur precursors from different syringes into a heated solution of cores in TOPO. The slow speed prevents the formation of ZnS cores. Instead, the precursors attach to the existing dots.

3.2.3   Results

The procedure described here produces dots peaked at 609 ± 3 nm. The consistency of the peak is largely dependent on environmental factors such as chemical impurities, atmospheric humidity, and chemical technique. A skilled chemist can consistently produce dots at 609 nm with 30 nm FWHM spectrum.

Figures 3-6 and 3-7 show the absorption and emission spectra of the dots before and after overcoating.
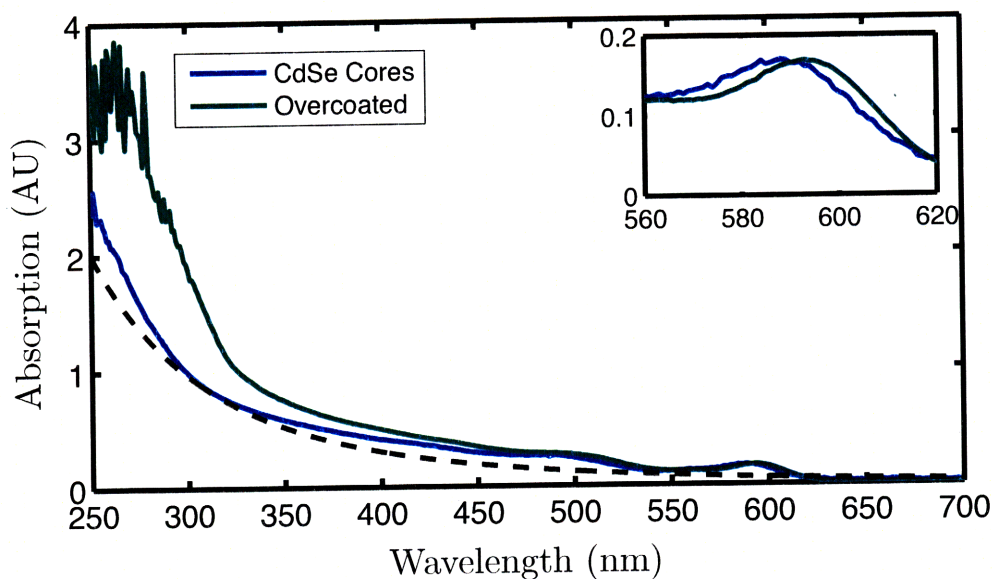
Figure 3-6: Absorption of (CdSe)ZnS QDs before and after overcoating. The overcoating leads to a redshift in absorption from 588 to 593 nm (see inset). Additionally, the low-wavelength absorption (above the bandgap of ZnS) increases due to the increased cross-sectional area of the dot. The Rayleigh scattering envelope (see Section 4.1.1) is indicated with a black dashed line.
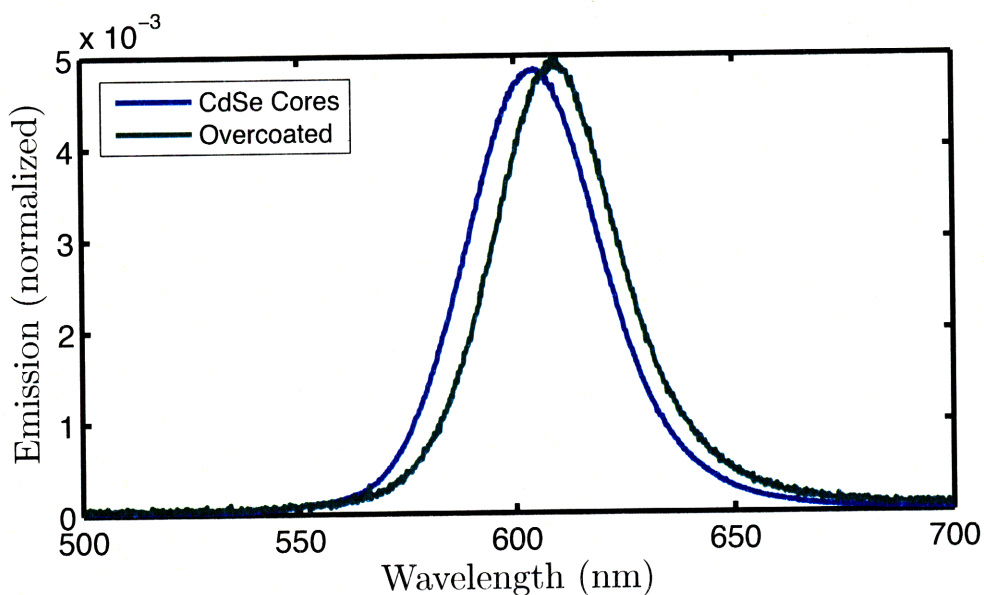

Figure 3-7: Emission of (CdSe)ZnS QDs before and after overcoating. Overcoating causes a redshift from 604 to 609 nm peak emission and slight narrowing of peak. Emission is normalized to a photon count of 1. Comparing to Figure 3-6, we measure a Stokes shift of 16 nm, which is uncharacteristically large for QDs.

Chapter 4

Device Fabrication Efforts

This chapter presents a chronological list of failed ideas in our efforts to fabricate a working device. Implementation efforts have been stymied by high attenuations of waveguide materials at the 3 eV excitation. Our application of guided optics is unique. Research is focused on signal transmission, not power transmission. Absolute energy losses are tolerated to the extent that noise pollution is minimal.

At first glance, a waveguide with high transparency in the visible spectrum should be easily fabricated. As Table 4.1 shows, the highest energy vibrational transitions remain in the near IR. Their resonances are still too low to affect the transmission of visible frequencies. On the other hand, high energy electronic transitions lie in the deep UV [47]—far beyond our 3 eV excitation. Then what is the difficulty?

A brief historical note. Long range signal transmission uses silica fibers as pure monolithic strands of silica can be easily fabricated. Losses in fused-silica fibers are dominated in the near IR by dissolved hydroxide (OH) groups and in the UV by Rayleigh scattering (see Figure 4-1(a)). There is a broad minimum in the near IR, with an absolute minimum at 1550 nm where the theoretical attenuation is $\alpha = 0.16$ dB/km. Local minima appear at 850 and 1310 nm. These three wavelengths, as well as 1300, are the standard telecommunications wavelengths.

As one might expect, optimizing for attenuation in silica left engineers scrambling to solve other problems. The first was economical light sources, and diode lasers were the solution. Today these wavelengths are once again presenting problems. Lately,

optical interconnects have been miniaturized from overseas transmission to on-chip interconnects. For ease of fabrication, new materials are being utilized including organic polymers and metal-oxides [45, 6]. These are the same materials that interest us. Because near IR wavelengths have been used historically, these new materials must propagate light at those frequencies. Unfortunately, these new materials are not near as efficient as silica for the near IR.

Contemporary waveguide research, then, has three parts: (1) create a new material or processing techniques, (2) fabricate useful waveguide structures such as a 3 dB splitter or a ring-resonator filter, and (3) measure the attenuation at the telecommunications wavelengths (800, 1300, and 1550 nm). The visible range is ignored and new materials are not engineered for visible transparency.

We have found that popular waveguide materials have significant losses in the blue. This observation is discussed below.

4.1   Criteria Overview

This chapter presents the material sets that we have investigated. We searched for materials that fit the following criteria [45, 6]:

- High transparency at 400 nm

- High chemical and environmental stability

- High refractive index controllability

- Good processability

4.1.1   High transparency at 400 nm

The transparency (or lack thereof) of a material is a result of bond resonances that occur at optical frequencies or scattering from localized impurities.

Attenuation from Vibrionic Resonances

Examples of typical vibrational resonances are listed in Table 4.1. We see that this table is particularly relevant for telecommunications wavelengths, and that much effort has been expended to avoid the C−H 1300 nm absorption peak when fabricating new materials. For instance, through perfluorination, hydrogens are replaced with highly-electronegative fluorine. Perfluroination shifts the nominal bond absorption peak above the communications wavelengths. Such modifications have trade-offs; perfluorinated polymers have lower glass transition temperatures [45] and lower optical densities [51].

Importantly, Table 4.1 does not list significant absorption peaks in the visible. The vibrational resonances of organic bonds are too low in energy to affect the transmission of visible frequencies. Rather, it is electronic resonances and Rayleigh scattering that attenuate visible frequencies.

Attenuation from Electronic Transitions

Take, for instance, the C=C bond, which does not even appear on in Table 4.1. The vibrational energies lie above 2000 nm. Furthermore, in ethylene, the $\pi \rightarrow \pi^*$ transition occurs at 171 nm, which is far below our excitation wavelength [47]. However, this energy redshifts for conjugated double bonds. In buta-1,3-diene ($H_2C=CH−CH=CH_2$), the $\pi \rightarrow \pi^*$ transition shifts to 217 nm, and in hexa-1,3,5-triene, it is at 258 nm [11]. Clearly if we work with low molecular weight polyethylene or an aromatic polymer we must be careful about this bond. Furthermore, this absorption bleeds exponentially into higher wavelengths via the Urbach tail at room temperatures.

Attenuation from Rayleigh Scattering

Visible transmission also suffers from Rayleigh scattering. Random localized impurities and random density inhomogeneities in the polymer act as scattering centers. As mentioned in Section 2.1.1, Equation 2.1 simplifies to Equation 2.2 only when the variations in the dielectric constant occur adiabatically. For localized impurities,

the vector potential couples to the scalar potential creating a polarization density $\mathcal{P}$ which corresponds to a source of radiation proportional to $\partial^2 \mathcal{P}/\partial t^2 = -\omega^2 \mathcal{P}$. Thus the scattered field is proportional to ω^2, and the intensity goes as $\omega^4 = 1/\lambda^4$. This is Rayleigh's famous inverse fourth-power law [38]. It is valid for scattering centers with radii much smaller than λ. (Mie scattering dominates for $a \geq \lambda$.)

In summary, we need to carefully select our polymers to avoid absorption at the excitation wavelength due to electronic transitions of electrons in our polymer.

Table 4.1: Positions and relative strengths of fundamental and overtone absorption due to vibrational modes of common optical polymer bonds. Wavelengths are in nanometers and strengths are normalized to the first C−H absorption peak. The C=C absorption peak and overtones are not listed, but all lie above 2000 nm. From [15].

Absorption	C−H λ	C−H I/I_o	C−D λ	C−D I/I_o	C−F λ	C−F I/I_o	C=O λ	C=O I/I_o	O−H λ	O−H I/I_o
ν_1	3390	1 (def.)	4484	0.4	8000	40	5417	16	2818	10^{-1}
ν_2	1729	10^{-2}	2276	10^{-2}	4016	10^{-1}	2727	10^{-1}	1438	10^{-2}
ν_3	1176	10^{-3}	1541	10^{-3}	2688	10^{-2}	1830	10^{-2}	979	10^{-3}
ν_4	901	10^{-4}	1174	10^{-4}	2024	10^{-4}	1382	10^{-4}	750	10^{-4}
ν_5	736	10^{-5}	954	10^{-5}	1626	10^{-6}	1113	10^{-5}	613	10^{-5}
ν_6	627	10^{-5}	808	10^{-6}	1361	10^{-7}	934	10^{-7}	523	10^{-6}
ν_7			704	10^{-7}	1171	10^{-9}	806	10^{-8}		
ν_3					1029	10^{-10}				

4.1.2 High Chemical and Environmental Stability

Our material set must be stable against both chemical and environmental (thermal and physical) degradation. For instance, it would behoove us to choose a polymer with low water absorption. We also have expectations that the device survive outside the laboratory and be robust against physical damage.

Most materials fulfill these requirements, although the glass transition temperature, T_g, is of particular concern. If we butt-couple the excitation LED to our device, we do not want the device to melt. Additionally, a device that swells due to thermal expansion will change the delicate refractive index matching conditions that we strive to engineer. Fortunately dn/dT for common polymers is on the order of 10^{-4} °C^{-1}.

4.1.3 High Refractive Index Controllability

The material should have some mechanism to control the refractive index. In particular, we should be able to raise the index of the core above the index of the cladding. The refractive index of polymers can vary from lower than 1.3 to higher than 1.6, depending on chemical elements and the moieties in the polymeric chain structure. In general, perfluorinated polymers have low optical densities ($n \sim 1.3$), aliphatics fill the middle of the range, and aromatic groups and chlorine make polymers optically denser [51].

It is advantageous that the refractive index of polymers can be easily and precisely tuned through both copolymerization of two or more monomers, and by controlling the degree of cross-linking. We demonstrate both of these effects below. A drawback of this approach is that the refractive index shows batch-to-batch variability [51, 3].

4.1.4 Good Processability

Our final criteria asks that our material set be easily processed. Typical processing steps include spin-coating, photo lithography, reactive ion etching, chemical etching, milling, molding, stamping, and nano-imprinting.

In our device, we require good adhesion to glass, silicon, and other polymers,

and the ability to spin coat the polymer onto such substrates. We require that our polymer be easily patterned into a waveguide structure, preferably through photolithography. We also searched for materials that we could stamp or imprint with a periodic structure.

In addition to selecting a core material, we also have grappled with the problem of finding a material in which to stabilize the quantum dots. Specifically for the cladding, we require a material that will accept a high loading fraction of QDs without luminescence quenching or phase-segregation. Sol-gel was used initially. However, its low repeatability and frustrating yield prompted us to cast about for a better solution.

We considered both drop-casting, dip-coating, and spin-coating deposition methods for the dot cladding layer. Drop casting is simple and easily performed with an inject printer. We were also interested in identifying a material compatible with spinning dots so that a core could be deposited on top of the dots, rather than on top of a substrate.

4.2 Silica Fiber and Sol-Gel

Our original material set was an silica fiber and silica sol-gel. Silica fibers were surveyed above. An extensive overview of the sol-gel process is given by Hench and West [17]. Briefly, sol-gel chemistry is the study of colloidal particulates or macroscopically large molecules of metal oxides. When a metal alkoxide precursor is heated, a metal-oxide matrix is formed via hydrolysis and subsequent condensation. If that matrix is silicon dioxide, it evident that sol-gel chemistry provides a method to chemically synthesize glass at low temperatures. Commercial products are available, such as Accuglass 111 "Spin On Glass" by Honeywell.

4.2.1 Experimental

The fiber was a polymer clad 200 micron low OH silica core from Polymicro Technologies. The cladding was mechanically striped so that the bare core was exposed. The transmission of the unaltered fiber is depicted in Figure 4-1, where it is also

compared to the high OH fiber. Here Rayleigh scattering limits transmission at the UV end of the spectrum while dissolved hydroxide (OH) groups limit transmission in the infrared [38].

The silica sol-gel was synthesized via the Stöber process, which involves the hydrolysis and subsequent condensation of a silicon alkoxide such as tetraethylorthosilica (TEOS) in a basic solution of ethanol and water [5]. The reaction is illustrated in Figure 4-2.

Quantum dots were prepared as in Section 3.2. A cap exchange was performed to replace native TOP and TOPO capping ligands with 5-amino-1-pentanol (AP) for subsequent solubility in ethanol as well as 3-aminopropyltrimethoxysilane (APS) for bonding with the silica matrix. A mixture of the sol-gel precursor (TEOS) in ethanol, QDs, and ammonium hydroxide were prepared in an anhydrous nitrogen environment.

The sol-gel/QD solution was removed to air and the core was dip-coated in the sol-gel/QD mixture. Finally the sol-gel was gelled by hotplate contact at 120 °C for two minutes. The elevated temperature together with moisture in the air causes rapid hydrolysis of the siloxane precursor, which subsequently condenses to form a thin layer of silica.

4.2.2   Results and Discussion

We started with this material set for proof-of-concept. In Figure 4-3, we see that our evanescent-coupling theory work in practice.

However, we cannot feed the fiber back on itself to recycle the excitation light as proposed. Furthermore, the sol-gel/QD synthesis is highly fickle and results are not repeatable on-demand. Several attempts were required to create the device shown.
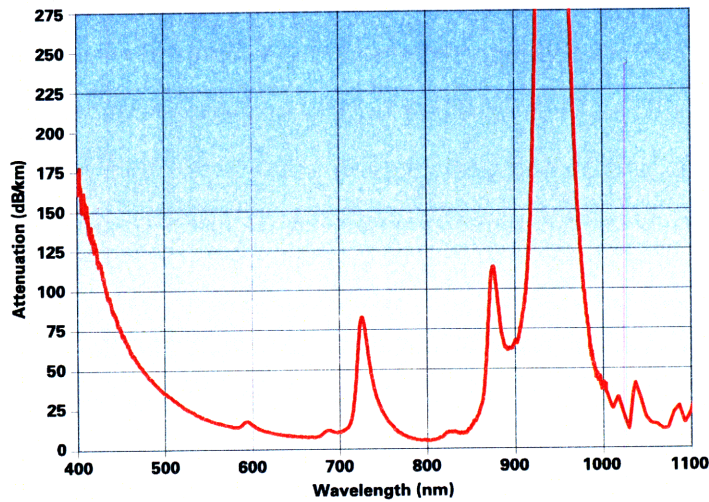
For the next generation of the device, we focused on polymeric core waveguides because these are easy to form into the desired Q-shape.
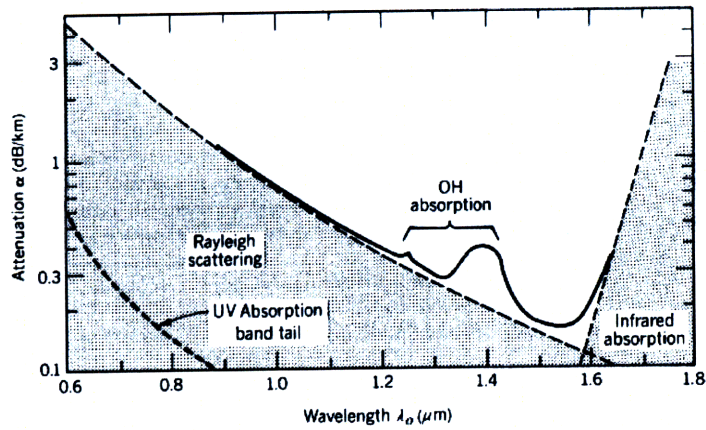
(a) Theoretical [38]
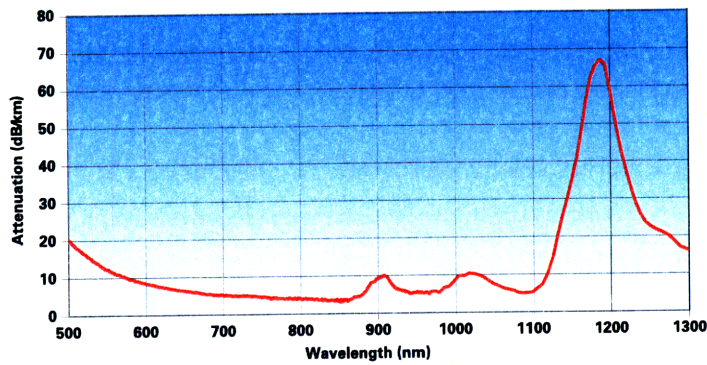
(b) Low OH Silica (Polymicro Tech)

(c) High OH Silica (Polymicro Tech)

Figure 4-1: Comparison of the transmission for low OH and high OH silica cores used for this thesis. The O−H content refers to hydroxide groups dissolved in the silica. (The silica preform absorbs water during the drawing of the fiber.) We expect (and observe) that the dissolved hydroxide groups will have absorption peaks at 613, 750, and 979 nm. (see Table 4.1). Rayleigh scattering limits transmission in the UV.
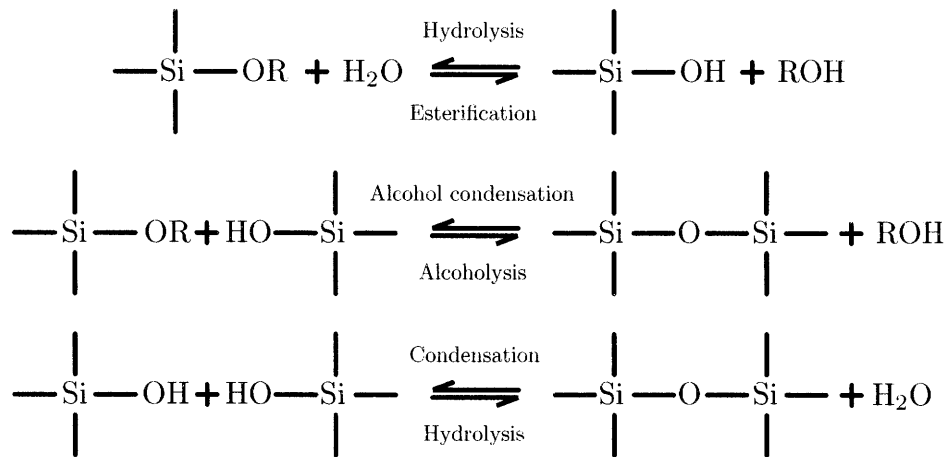
$$—\overset{|}{\underset{|}{Si}}—OR \;+\; H_2O \;\overset{\text{Hydrolysis}}{\underset{\text{Esterification}}{\rightleftharpoons}}\; —\overset{|}{\underset{|}{Si}}—OH \;+\; ROH$$

$$—\overset{|}{\underset{|}{Si}}—OR + HO—\overset{|}{\underset{|}{Si}}— \;\overset{\text{Alcohol condensation}}{\underset{\text{Alcoholysis}}{\rightleftharpoons}}\; —\overset{|}{\underset{|}{Si}}—O—\overset{|}{\underset{|}{Si}}— \;+\; ROH$$

$$—\overset{|}{\underset{|}{Si}}—OH + HO—\overset{|}{\underset{|}{Si}}— \;\overset{\text{Condensation}}{\underset{\text{Hydrolysis}}{\rightleftharpoons}}\; —\overset{|}{\underset{|}{Si}}—O—\overset{|}{\underset{|}{Si}}— \;+\; H_2O$$

Figure 4-2: Illustration of the Stöber process of sol-gel synthesis. Hydrolysis of the silicon alkoxide moiety, as reflected in the first reaction, is the first step towards the formation of a silica matrix. A small amount of ammonium hydroxide is used to catalyze the hydrolysis reaction, and the reaction rate can be controlled through the pH of the solvent environment.

4.3 NOA-63

We decided to try a commercial UV-curable polymer, Norland Optical Adhesive (NOA) 63 from Norland Products. NOA-63 is a urethane-related polymer cured by mercapto-related crosslinking reagents and UV light. It was originally developed as an optical adhesive and has excellent optical properties over a wide spectral range. The refractive index is 1.56 and transmission is above 98% between 360 and 1260 nm. Unknown at the time of this experiment, NOA-63 loses its adhesion to glass above 60 °C [34].

In literature, NOA-63 is used in conjunction with PDMS and SU-8 to form optical waveguides [7]. We wanted to mold NOA-63 into the Q-shaped waveguide.

4.3.1 Experimental

Our plan was to mold the NOA-63 using an aluminum mold and glass substrate. The aluminum mold, shown in Figure 4-4 was designed in SolidWorks. Due to manufacturing constraints, the waveguide core was 200 microns thick.

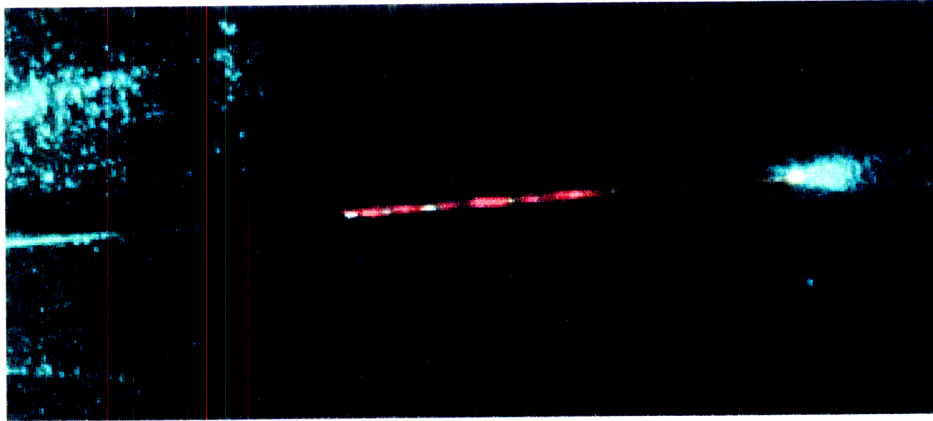This master was never produced for the following reason. In tests, 2 mil aluminum

Figure 4-3: Picture of luminescent fiber pumped by a 514 nm laser. The evanescent field of the propagating modes couples with QDs embedded in a silica sol-gel, which emit at 609 nm. Only a small fraction of the pump light couples into the QDs; the rest spills out at the end of the fiber. Photo by Cliff R. Wong.
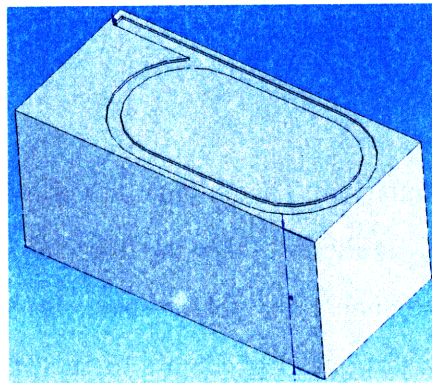

Figure 4-4: An aluminum mold was designed in Solid Works. The core groove is 200 microns deep.

shims were used to separate two glass slides with NOA-63 in the middle. The NOA-63 was then cured with UV exposure. It was discovered that NOA-63 is highly adhesive to glass and aluminum. Attempts to decrease the adhesion to these surface were not successful.

4.3.2 Results and Discussion

NOA-63 was abandoned after its adhesion proved problematic. In hindsight, knowing what we know now, NOA-63 would have been workable. It is known that NOA-63

does not adhere to PDMS, for instance; a mold could be made in PDMS from a silicon master.

4.4 SU-8

Fresh off NOA-63, a sticky polymer, the next material was chosen for its ease of processing. SU-8 is a commercial negative tone epoxy photoresist from Microchem. Because of its chemical and physical stability, it is frequently used as a permanent resist in both optical and MEMS applications [43]. The polymer has many desirable properties, such as high refractive index, good adhesion to substrate, optical transparency in the visible, and high glass transition and high thermal decomposition temperatures [43].

Chemical Discussion

We chose the SU-8 3050 formulation. The polymer is a polyglycidyl ether of Bisphenol A. The photoresist derives its stability and name from the eight epoxy groups on the molecule (see Figure 4-5). When fully polymerized, SU-8 is a highly cross-linked polymer matrix. The two additional ingredients in the photoresist are a photoacid that catalyzes the polymerization by destabilizing the epoxy groups, and a solvent. Both cyclopentanone and γ-butryolactone (GBL) are used in SU-8 formulations; our batch used cyclopentanone.

The SU-8 solution is spun onto glass during which most of the solvent evaporates leaving a tacky film. A prebake step removes the remaining solvent; the resulting film is monomeric and easily washes off in acetone. The film is then exposed to UV, which generates a Lewis acid from the triarylium-sulfonium salt. The resulting acidity catalyzes the cationic polymerization of SU-8 during the post-exposure bake. Obscured areas where acid was not generated do not polymerize. These monomeric islands can be rinsed away in the development step.
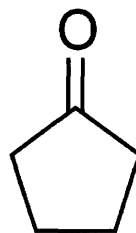
We can decrease the index of SU-8 by mixing Bisphenol A digylicdyl ether. This additive decreases the cross-linking and thus the optical density of the resulting poly-
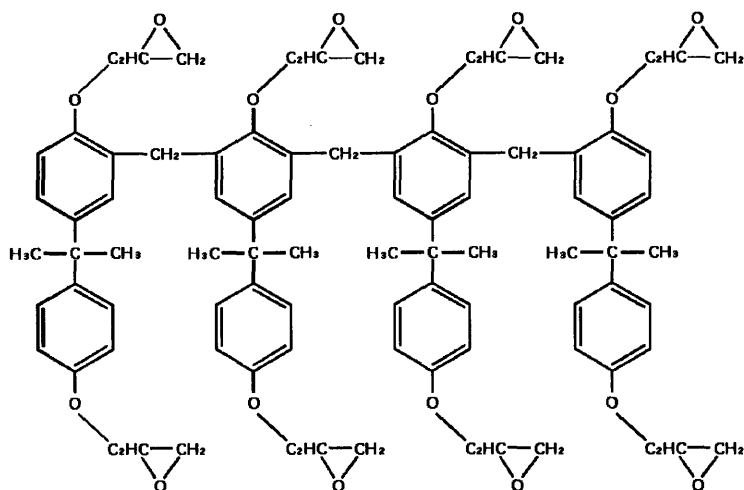
(a) SU-8 Monomer
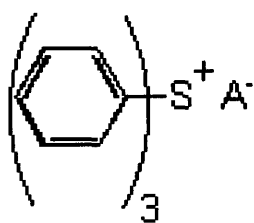
(b) Photoacid

(c) Solvent

Figure 4-5: Chemicals in SU-8 3000. The monomer is a polyglycidyl ether of Bisphenol A with eight epoxy groups. The photo-initiator is a photo-generated Lewis acid, triarylium-sulfonium salt. The solvent of our batch is aprotic cyclopentanone. γ-Butryolactone (GBL) is used in some SU-8 formulations.

mer [24].

4.4.1 Experimental

Procedures for 8 micron film

1. **Cleaning** We used 1 mm Electroverre float glass from Erie Scientific. The substrates were rinsed with soap, sonicated in soap, sonicated in water, sonicated in acetone, and finally immersed in boiling isopropanol. Clean substrates were treated with oxygen plasma immediately before spin coating.

2. **SU-8 Dilution** The stock SU-8 3050 solution was diluted in cyclopentanone in a ratio of 32. g of solvent to 100. g of stock SU-8 to decrease the viscosity and resulting film thickness. Whereas stock SU-8 is 72.5% solids by mass, our diluted SU-8 was 55%.

3. **Spin Coat Deposition** Diluted SU-8 was spun in a multistep process, 600 rpm, at 100 rpm/s ramp for 5 seconds, and then 4000 rpm at 600 rpm/s ramp for 30 seconds. The resulting film was smooth.

4. **Pre-Exposure Bake** The substrate with freshly spun film was exposed to a 95 °C hotplate for 6 minutes to fully evaporate residual solvent. The sample was cooled afterwards for 10 minutes.

5. **Exposure** We exposed the SU-8 using a transparency mask in contact with the SU-8. During removal, the transparency mask tended to introduce pits into the surface of the guide. We did not use any color filter, although it is recommended that a high pass filter at 365 nm be use for higher contrast results. For Bulovic lab users, the correct (arbitrary) exposure units are 20.

6. **Post-Exposure Bake** The exposed film was heated for 3 minutes at 95 °C on a hot plate to polymerize the SU-8. The sample was cooled afterward for 10 minutes.
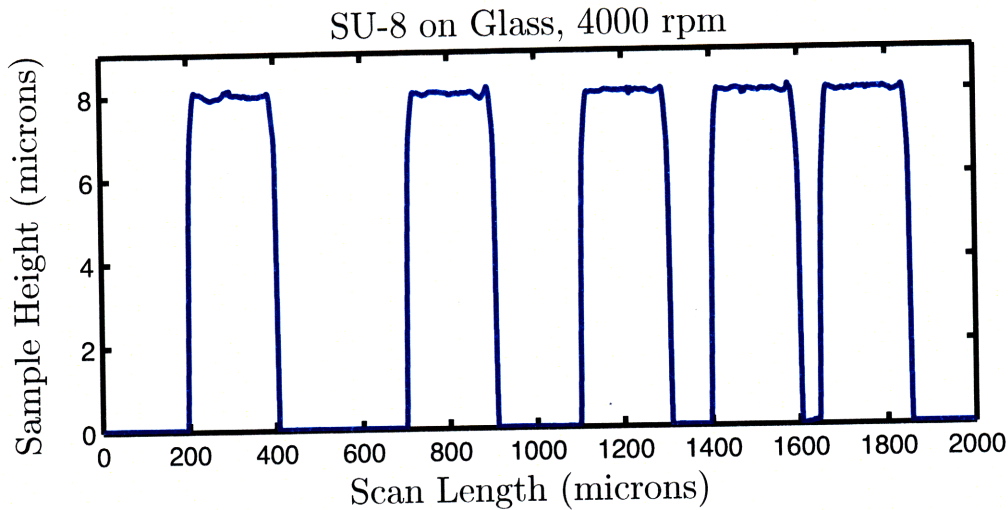
Figure 4-6: Film profile resulting from the optimized procedures above. The film height is 8 microns.

7. **Development** Lastly, we developed the samples for 30 seconds in SU-8 developer, a strong alcohol. The development was quenched with isopropanol.

4.4.2 Results and Discussion

SU-8 is a great material for quickly and reliably fabricating intricate structures. However, it has high optical attenuation in the blue part of the spectrum and cannot be use for our purposes. We see from Figure 4-9, that the attenuation at 400 nm is 17 dB/cm. This measurement matches the compilation of [40], which is reproduced in Figure 4-10.

Figure 4-10 is one to strike fear in the hearts of men. A low-loss polymer waveguide is "only" 1 dB/cm in the visible. Contrast this with silica fibers, where losses are measured in dB/km. If our waveguide is 3 cm in circumference, we would lose half of our power to intrinsic losses.

We conclude that the attenuation due to the dots must be much greater than the intrinsic attenuation of the guide. Because the attenuation of the dots is about 1 dB/cm, we desire a waveguide with losses on the order of 0.1 dB/cm or better.
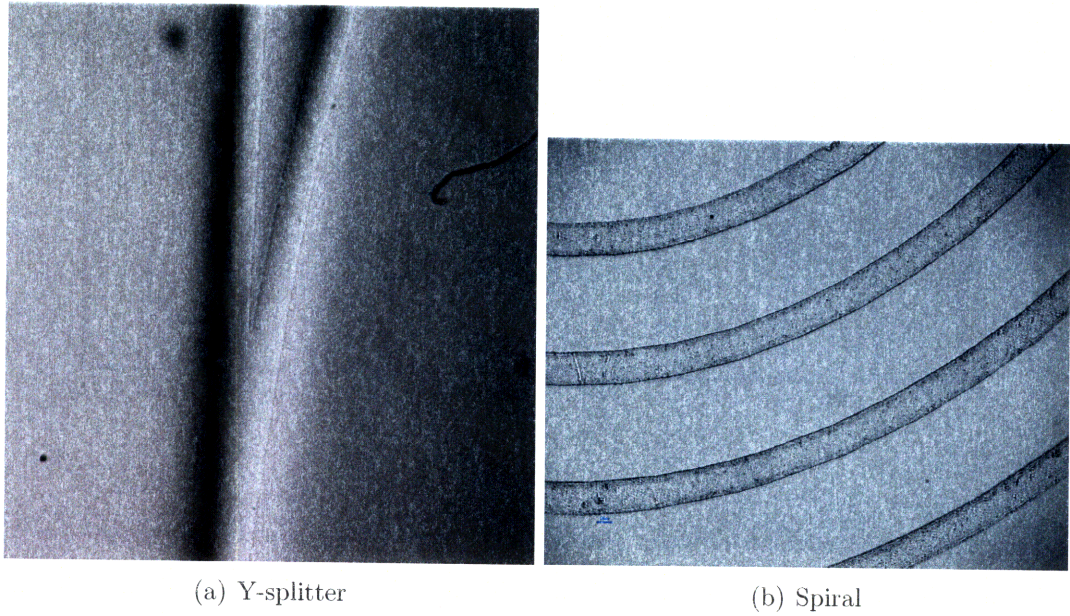
(a) Y-splitter

(b) Spiral

Figure 4-7: Waveguides fabricated from SU-8. Figure (a) shows a y-split with a top cladding layer; figure (b) shows a spiral guide without cladding.
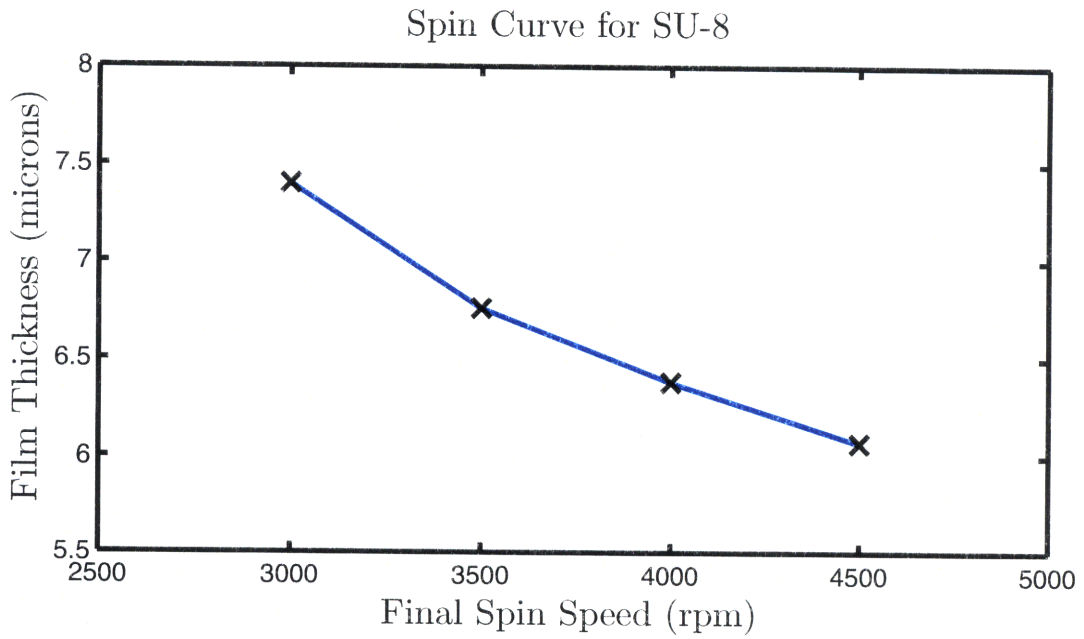

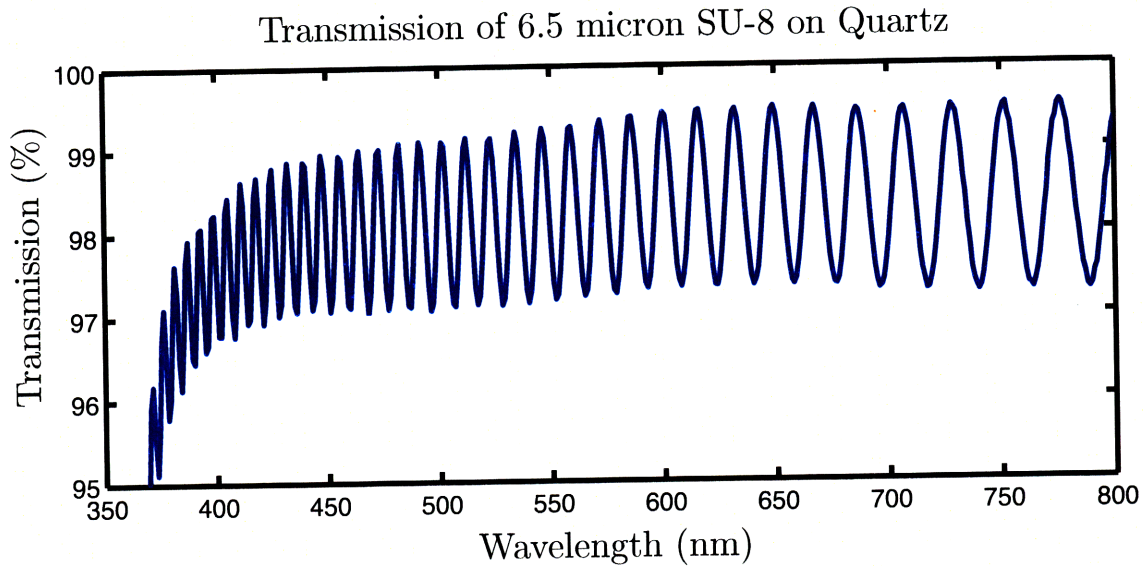Figure 4-8: Spin curve for SU-8 photoresist.

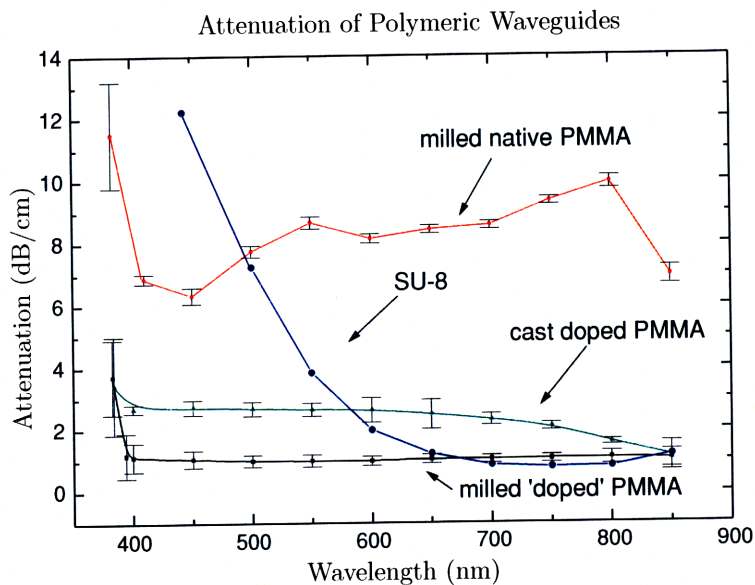Figure 4-9: Transmission of SU-8 for the visible spectrum.

Figure 4-10: Attenuation of various polymer waveguides by wavelength, from [40]. We observe that most polymer waveguides attenuate at about 1 dB/cm in the visible.

4.5 Spun PMMA and Polystyrene

This section details our search for a low-loss polymer. Specifically, we are searching for polymer that has attenuations of 0.1 dB/cm or better.

Motivated by researchers in Swager's group, we looked at poly methyl-methacrylate (PMMA), otherwise known as Plexiglas, and polystyrene (PSt), the polymer used for everything from packing peanuts to grocery bags. Both of these materials can be dissolved in a variety of solvents and spun onto glass and silicon.

4.5.1 Experimental

Dissolving polymers turns out to be as much art as science. Some polymers want polar solvent, some don't, and a third class is indifferent. Some polymers want aprotic solvents, others want protic solvents. Sonication sometimes helps. Heat is sometimes helpful but in all other cases disastrous. The only sure thing that speeds dissolution is stirring.

4.5.2 Results and Discussion

The transmission curves for spun PSt and PMMA are shown in Figure 4-11. The results are not encouraging as even a few microns of polymer drops the transmission below that of the naked glass significantly.

4.6 DUV Treatment of PMMA

Our final thrust has been the deep-ultraviolet treatment of PMMA. It was observed by Tomlinson [42] that deep UV treatment of PMMA caused a local increase in the refractive index due to densification of the polymer. The mechanism for this increase was later explained by Bowden [3] as follows. The deep UV photons cause the oxidation residual monomer into peruvates. (Because of the radical polymerization of MMA, up to 20% of the monomer will be unreacted.) These peruvate products can then act as radical initiators; upon annealing, some of the residual monomer will
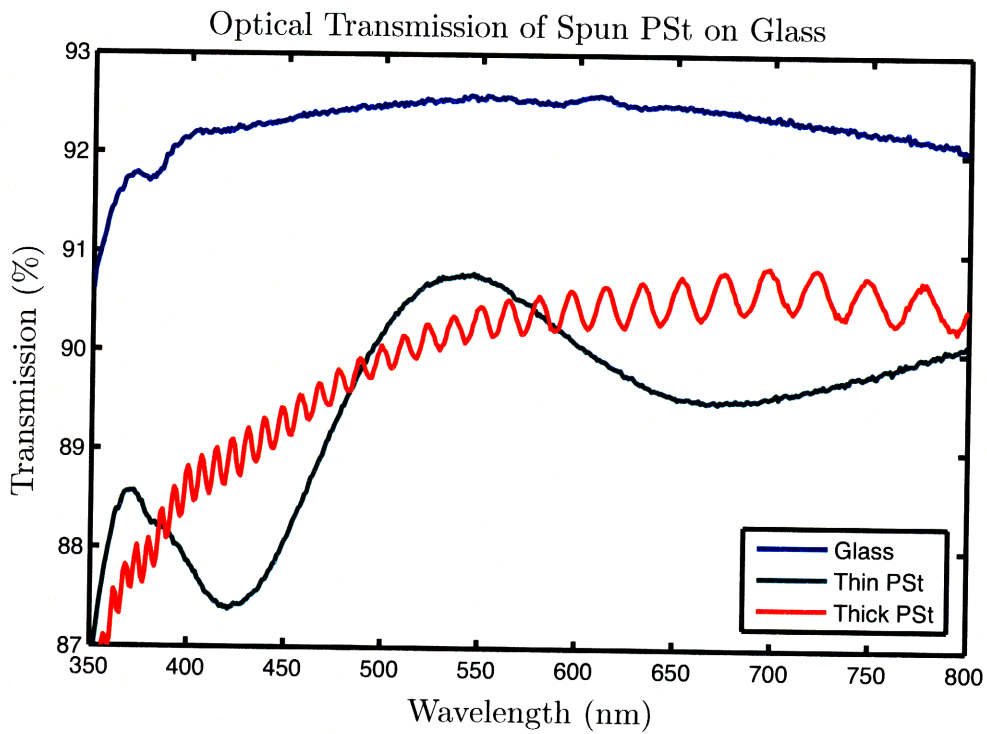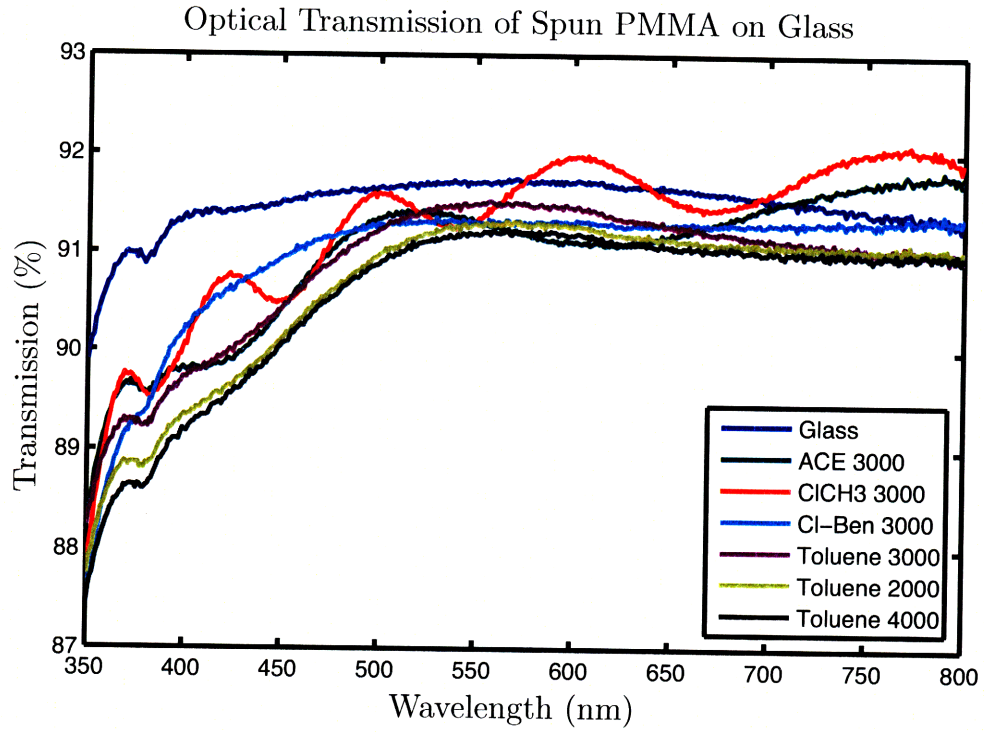
Figure 4-11: Transmission through thin films of PMMA and PSt. The attenuation at 400 (as compared to the naked glass) is too large for our application to be successful.

polymerize leading to a densification of the PMMA. The residual monomer has been tracked by [28], and shown to be reduced upon deep UV + annealing treatment. The index increase is about 0.008.

Recently labs have been using this phenonmenon to fabricate waveguides through photoexposure [36, 18, 37, 20]. They have reported good results will limited attenuations. We are hopeful this PMMA success is due to better optical characteristics than the spun films demonstrate.

4.6.1 Experimental

We use Hesa-glas PMMA substrates from G-S Optics. These are precision slabs of PMMA. The substrates are exposed to a Xenon flash lamp for a total of 2 minutes in a nitrogen environment. To avoid heating the substrate, the exposure is broken up into four 30 second segments. The PMMA substrates are then annealed at 55 °C for 24 hours to densify the exposed areas. The exposed areas are visible to the naked eye as 10 micron depressions on the surface of the substrate.

The result is a surface slab waveguide a few microns deep in the PMMA. The core is densified PMMA, with an index approximately 0.008 higher than the cladding.

A micro prism is attached to the surface of the guide and light can be prism coupled into the guide. Although we are currently in the process of quantifying this technique, early results are pictured in Figure 4-12.
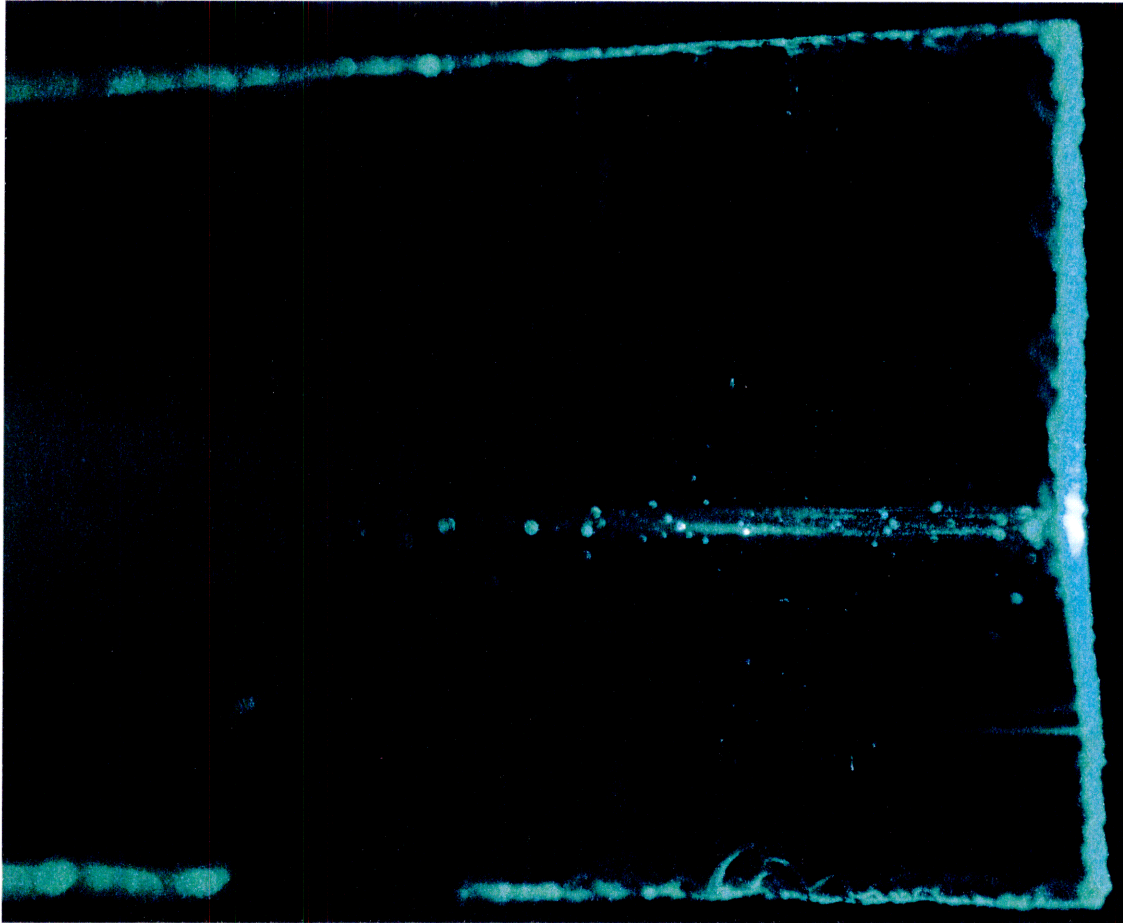
Figure 4-12: A PMMA waveguide defined by deep UV exposure. The waveguide is on the top few microns of the PMMA substrate.

Chapter 5

Conclusions and Future Work

In the introductory chapter we cited the growing demand for energy, including energy for artificial lighting. It is timely that progressive states like California are debating banning the sales of incandescent fixtures entirely [46].

There are two barriers to adoption of SSL. The first is cost. Cost of new fixtures and new bulbs deters consumers. One estimate is as high as $400 per room to install LED lighting [29]. The second is color; incandescent bulbs look better. People prefer the good color halogens for reading [32]. The first concern will evaporate overtime as prices drop. The second concern, however, will not disappear without concentrated research.

Quantum dots are an obvious choice of luminescent material. Specific advantages include their range of emission frequencies, their greater stability, and their high density of absorbing states. However, previous efforts to utilize quantum dots have resulted in poor efficiencies related to the reabsorption problem. Reabsorption can be avoided with either (1) dilute assemblies, or (2) thin films. However, neither of these geometries will completely attenuate the backlight. To the extent that the backlight is undesired, QDs were, in the old design, not an ideal choice.

We have presented a novel device structure in which the excitation was orthogonal to the emission and the two were evanescently-coupled. The design eliminated the need to completely attenuate the backlight and breathed new life into thin film quantum dot photoluminescence in applications where the backlight should be completely

converted.

Chapter 2 gave a detailed theoretical foundation for evanescently-coupled photo-luminescent devices. It was discovered that the desired four-layer structure had a narrowly defined range of values for which it was both single mode and evanescent in the cladding. Multimode guides were also examined and attractive because of the relatively unconstrained design parameters. But we concluded that the low cladding energy of multimode guides was undesirable. The recommendation was to fabricate a single mode device, with the recognition that a multimode device was an acceptable fallback.

We overviewed the physics of the CdSe nanocrystal to better understand the optical properties of quantum dots in Chapter 3. This overview offered a detailed explanation of QD synthesis including the overcoating process. Emission and absorption of naked and overcoated CdSe cores were presented. The small Stoke's shift of QDs is seen in this data.

Finally in Chapter 4 we detailed several techniques to fabricate the proposed device. We discovered that few polymeric materials transmit blue light without attenuation, and chemical explanations for this attenuation were proposed. The measured attenuation of different waveguide materials was listed. We concluded that fused silica is the best core material.

Future Work

While this thesis has laid the theoretical groundwork and begun work on the fabrication, it has made little progress toward a Q-shaped guide with reasonable losses in the blue. Much of the chemistry has been worked out, but time must be invested in further experimentation to develop expertise in high-quality polymeric waveguide fabrication. Furthermore, careful selection of the proper photonic crystal structure should enhance the light emission (and external efficiency) of the device. It is an area beyond my expertise.

In the abstract, the possibility to spatially separate the excitation from the emission was mentioned. For instance, a common the excitation source could be located

outside of buildings; any heat dissipated by the source would not fight against the air conditioners.

Additionally, while this thesis sells the idea of white lighting, quantum dots and this design could be used in any application requiring broad illumination with a precise spectrum. For instance, a light could be tailored for chloroform absorption. Special growing lamps in plant nurseries are (1) inefficient, (2) expensive and (3) contain mercury—with our device, only beneficial wavelengths would be produced and the bulbs would never burn out.

Bibliography

[1] S. Adachi. *Handbook on Physical Properties of Semiconductors*, chapter 13, pages 329–336. Springer, 2004.

[2] R. Adar, C.H. Henry, M.A. Milbrodt, and R.C. Kistler. Phase Coherence of Optical Waveguides. *Journal of Lightwave Technology*, 12(4):603–606, 1994.

[3] M.J. Bowden, E. A. Chandross, and I.P. Kaminow. Mechanism of the photoinduced refractive index increase in polymethyl methacrylate. *Applied Optics*, 13(1):112–117, 1974.

[4] W. K. Burns and A. F. Milton. Mode conversion in planar-dielectric separating waveguides. *IEEE Journal of Quantum Electronics*, 11(1):32–39, 1975.

[5] Yinthai Chan. *The Physics and Chemistry of Semiconductor Nanocrystals in Sol-gel Derived Optical Microcavities*. PhD dissertation, Massachusetts Institute of Technology, Department of Chemistry, 2006.

[6] Yin-Jung Chang. *Optical Interconnects for In-Plane High-Speed Signal Distribution at 10 Gb/s: Analysis and Demonstration*. PhD dissertation, Georgia Institute of Technology, School of Electrical and Computer Engineering, 2006.

[7] D A Chang-Yen and B K Gale. Design, fabrication, and packaging of a practical multianalyte-capable optical biosensor. *J. Microlith., Microfab., Microsyst.*, 5(2):021105, 2006.

[8] K.S. Chiang. Analysis of rectangular dielectric waveguides: Effective-index method with built-in perturbation correction. *Electronics Letters*, 28(4):388–390, 1992.

[9] K.S. Chiang. Analysis of effective-index method for vector modes of rectangular-core dielectric waveguides. *IEEE Transactions on Microwave Theory and Techniques*, 44(5):692–700, 1996.

[10] K.S. Chiang. Effective-index method with built-in perturbation correction for the vector modes of rectangular-core optical waveguides. *Journal of Lightwave Technology*, 17(4):716–722, 1999.

[11] Jim Clark. Uv-visible absorption spectra, 2007. Online; accessed 7-May-2008.

[12] G.N. de Bradander, J.T. Boyd, and G. Beheim. Integrated Optical Ring Resonator With Micromechanical Diaphragm for Pressure Sensing. *IEEE Photonics Technology Letters*, 6(5):671–673, May 1994.

[13] Al. L. Efros and M. Rosen. The electronic structure of semiconductor nanocrystals. *Annu. Rev. Mater. Sci.*, 30:475–521, August 2000.

[14] N. Ganesh, W. Zhang, P. C. Mathias, E. Chow, J A N T Soares, V Malyarchuk, A D Smith, and B T Cunningham. Enhanced fluorescence emission from quantum dots on a photonic crystal surface. *Nature Nanotechnology*, 2:515–520, 2007.

[15] W. Groh. Overtone absorption in macromolecules for polymer optical fibers. *Macromol. Chem.*, 189:2861–2874, 1988.

[16] Herman A. Haus. *Waves and Fields in Optoelectronics*, section 6.2–6.4, pages 163–178. CBLS, New Delhi, 2004.

[17] L L Hench and J K West. The Sol-Gel Process. *Chemical Review*, 90:33–72, 1990.

[18] P. Henzi, K. Bade, D.G. Rabus, and J. Mohr. Modification of polymethylmethacrylate by deep ultraviolet radiation and bromination for photonic applications. *Journal of Vacuum Science and Technology B*, 4(24):1755–1761, 2006.

[19] K.O. Hill and A. Watanabe. A Distributed-Feedback Side-Coupled Laser. *Optics Communications*, 5(5):389–393, 1972.

[20] Y. Ichihashi, P. Henzi, M. Bruendel, and J. Mohr. Polymer waveguides from alicyclic methacrylate copolymer fabricated by deep-uv exposure. *Optics Letters*, 32(4):379–381, 2007.

[21] John David Jackson. *Classical Electrodyanmics*, section 8.11, pages 359, 385–387. John Wiley and Sons, Inc., New York, third edition, 1999.

[22] J. J. Ju, J. Kim, J Y Do, M-S Kim, S K Park, S Park, and M-H Lee. Second-harmonic generation in periodically poled nonlinear polymer waveguides. *Optics Letters*, 29(1):89–91, 2004.

[23] J.H. Jung and T. Kinoshita. Periodically domain inverted poled polymer waveguide by two-step poling. *Jpn. J. Appl. Phys.*, 41(3A):1587–1588, 2002.

[24] J W Kang, J J Kim, J Kim, X Li, and M H Lee. Low-loss and thermally stable TE-mode selective polymer waveguide using photosensitive fluorinated polyimide. *IEEE Photonics Technology Letters*, 14:1297, 2002.

[25] A. Kobayashi, O.F. Sankey, S.M. Volz, and J.D. Dow. Semiempirical tight-binding band structures of wurtzite semiconductors: Aln, cds, cdse, zns, and zno. *Phys. Rev. B*, 28(2):935–945, 1983.